Chapter 3
Experimental Technique

In Sect. 3.1, a number of thermography and lock-in thermography approaches from literature are described and discussed, both steady-state and non-steady-state, showing the large variety of thermography measurement possibilities. Many of these systems are not called thermography but rather thermo-AFM, or photothermal or thermo-elastic investigations. But, in principle, they are all designed to measure lateral surface temperature distributions, and can be used to investigate also electronic components. At the end of this chapter, the figures of merit of different lock-in thermography systems are compared in terms of the pixel-related system noise density, defined in Sect. 2.6. In Sect. 3.2 the design philosopies of different commercial lock-in thermography systems are compared and typical test measurements are introduced. Since many novel techniques for investigating solar cells are working with homogeneous irradiation of light, in Sect. 3.3 different systems for illuminating the sample are compared. In Sect. 3.4 the application of solid immersion lenses for improving the spatial resolution of lock-in thermography investigations is described. Finally, Sect. 3.5 introduces the special demands of the realization of different non-thermal carrier density imaging techniques, which also make use of the illumination systems described in Sect. 3.3.

3.1 Different (Lock-in) Thermography Realizations

In the following, we will consider only thermographic techniques which are at least potentially able to produce an image of electrically generated internal heat sources in electronic components. This rules out any photoacoustic and photothermal techniques which are solely based on measuring the local surface heating produced by a pulsed laser spot. Before infrared (IR) imaging techniques will be discussed, a number of alternative thermography techniques will be reviewed. The most straightforward way of measuring the temperature of a device is to attach a temperature sensor to the surface in contact mode. Therefore, contact thermography is one of the most popular serial thermography approaches. Of course, contact thermography can only be a serially measuring technique, since a large parallel working array of contact sensors is impracticable. Most of the contact thermography approaches in

the literature are microscopic techniques aiming at a spatial resolution of 1 μm or below. Therefore they belong to the category of thermal atomic force microscopy (Thermo-AFM) techniques. The two dominant basic principles of electronic temperature measurements, the thermocouple and the resistance thermometer, have both been used on a microscopic scale. So Williams and Wickramasinghe [58] produced a special AFM tip by separating a metallic coating from the conducting conical tip via an insulating layer. Only at the tip apex these two conductors were in contact producing a thermocouple of about 100 nm in size. This tip actually worked in the non-contact mode with a constant temperature difference between tip and sample. By piezo-modulating the height at around 1 kHz, the thermosignal showed a distance-dependent a.c. signal component, which was used to stabilize the height position. The aim of this development was to establish a non-contacting AFM technique for insulating and soft materials rather than to map surface temperature distributions. Majumdar et al. [59] produced a larger thermocouple between two dissimilar wires by a capacitive discharging and subsequent electrochemical thinning. In a contacting AFM arrangement, they imaged steady-state surface temperature profiles of a GaAs MESFET with a temperature resolution of <100 mK and a spatial resolution of a few microns. Also Foster and Gmelin [60] have used a concentric thermocouple tip similar to that in [58] in a variable temperature AFM set-up to investigate the thermal properties of thin films in contact mode. This setup, too, was not used to investigate electronic components. One general problem of thermocouple tips is that they produce a very small d.c. signal. As mentioned above, using lock-in thermography greatly improves not only the sensitivity but also the spatial resolution in thermal investigations. If the tip is in close contact to an electronic device in a lock-in measurement, it is very hard to suppress capacitive coupling between the device driving voltage and the thermal tip signal. This may be one major reason why thermocouple-based AFM systems have rarely been used for investigating electronic components until now.

Resistive thermometers may be loaded and read out with a sufficiently high frequency a.c. current, leading to several advantages in comparison to thermocouples: First, if the resistor read-out frequency and the lock-in one are sufficiently wide apart, a capacitive coupling of the driving voltage into the temperature reading can be avoided. Second, the a.c. principle of measuring the resistance avoids the influence of the so-called $1/f$ noise, which is the dominating noise source in all d.c. amplifiers. Therefore a.c. driven resistors may be read out considerably more sensitively than d.c. driven ones. Finally, at least semiconductor-based NTC (negative temperature coefficient) thermistors show a temperature coefficient ten times higher than metal resistors do, which also favours a higher temperature resolution. Hammiche et al. [61] formed an STM tip from a loop of so-called Wollaston wire. This is a 5 μm diameter platin/rhodium wire embedded in a 75 μm diameter silver wire. At the loop tip, the silver is etched away leaving the Pt/Rh core of 150 μm in length, which may be used both as a micro resistivity temperature probe and as a micro heater. This tip was made commercially available by ThermoMicroscopes and was a part of the Micro-Thermal Analyzer of TA Instruments. After these companies have become part of Veeco [62], Scanning Thermal Microscopy (SThM) using the

Wollaston wire probe is now available for the Nanoscale Thermal Analysis (nTA) mode of the VITA option of the Innova-SPM of Veeco [62]. However, these set-ups are actually intended more for micro-thermal analysis such as differential scanning calorimetry or thermal conductivity mapping on polymers than for investigating electronic components. Nevertheless, a scanning thermal microscope of the Wollaston type has also been used for imaging current-induced heating in microelectronic structures with sub-micron resolution [63, 64]. Since the Wollaston wire does not show a sharp tip, the spatial resolution of this SThM system is limited to a few 100 nm. SThM with sub-100 nm spatial resolution and <0.1°C thermal resolution can be obtained by using a special microfabricated thermal probe, which was developed by Anasys Instruments [65]. Also this high-resolution SThM tip can be used in the VITA option of the Innova-SPM of VEECO [62]. Rangelow et al. [66] have published a thermal nano-probe based on a nanometer-sized filament, which was made by combining focused ion beam etching and a local electron beam deposition technique. The resistivity of this probe was read out in a 10 kHz a.c. bridge, realizing a thermal resolution of 1 mK. Similar to the system of Williams and Wickramasinghe [58], this system works in the non-contact mode with a constant temperature difference between sample and tip. It was used to measure the steady-state surface temperature distribution at the top of an implanted resistor with a spatial resolution below one micron. Although this tip is very fragile, and no details about necessary measurement times have been given up to now, this system also seems to be a promising thermo-AFM solutions for investigating electronic components. Its capabilities can even be improved considerably by using it in the lock-in thermography mode. Note, however, that all piezo-based thermo-AFM solutions imply one decisive problem: They hardly allow one to scan an image field much larger than $100 \times 100\,\mu m^2$. Thus, they usually do not allow one to scan a whole chip or even a larger component such as a solar cell.

In 1994 a macroscopic variant of this technique called Dynamic Precision Contact Thermography (DPCT [67]) was developed. Here a stepper-motor driven x-y-z table was used to scan a spring-loaded miniature thermistor point-by-point in contact mode across a macroscopic device like a solar cell. The spatial resolution of this system was only about 30 μm. The thermistor was read out very sensitively by a self-balancing a.c. bridge, and the two-phase correlation was performed by the computer after digitizing the temperature signal in four equidistant times per lock-in period. With this system, for the first time highly sensitive lock-in thermography investigations were performed at a lock-in frequency of 3 Hz. The thermal noise level, referred to the sample surface, was below 100 μK T-modulation amplitude at an integration time of 1 s per pixel, which was record-breaking at that time [68]. Thus, this system also allowed for the first time to investigate weak shunts in solar cells under forward bias. However, due to the serially measuring principle, the measurement time could not be reduced below several hours per image. Therefore this system has not gained wider popularity and was later replaced by an IR camera based system.

Besides the use of thermocouples and resistance thermometers there are a number of non-contacting techniques to measure surface temperature distributions. One

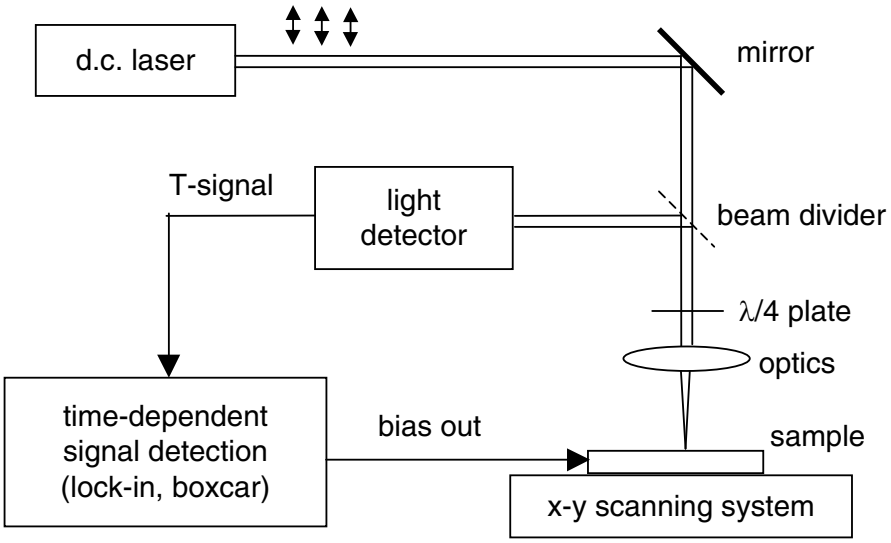

Fig. 3.1 Thermoreflectance measurement set-up for detecting internal heat sources

popular approach is the photothermal or thermoreflectance principle. It is based on the fact that the optical reflection coefficient of a reflecting surface is usually temperature-dependent. Typical temperature coefficients of the reflectivity of metals and semiconductors in the visible range are of the order of 10^{-5}–10^{-4}/K. For a well-defined reflecting surface, the intensity of a reflected laser beam is a measure of the surface temperature. As Fig. 3.1 shows, a typical thermoreflectance experiment on an electronic device comprises a d.c. laser producing a linearly polarized beam, a microscope objective, a beam splitter (usually combined with a $\lambda/4$ plate) for separating the incident and the reflected beam, and a mechanical scanning system. For example, Ju et al. [69] have measured temperature transients with an accuracy of 0.1 K and a spatial resolution of 0.6 μm in different positions of MOS transistors after pulsed biasing. Using a computer-controlled sample scanning system, Voigt et al. [70] performed lock-in thermoreflectance imaging at a modulation frequency of up to 30 kHz on electrically heated microconductors. Sensitivity limits have not been given here explicitly, but the power these structures dissipated was as high as 2 W. A very interesting "stroboscopic" camera-based photothermal imaging system for investigating high-frequency phenomena has been introduced by Grauby et al. [34]. They imaged the local reflectance of the sample surface by using a standard CCD camera operating at a frame rate of 40 Hz. Contrary to Fig. 3.1, however, not a d.c. light source was used for the illumination but an LED, which was amplitude-modulated at a frequency of (2 MHz + 10 Hz). The sample structures were electrically loaded to produce a surface temperature modulation of 2 MHz. Then the reflected optical signal is amplitude-modulated with the difference frequency of 10 Hz due to the heterodyne principle. With the given frame rate of 40 Hz, two-channel lock-in thermography with 4-point correlation has been

performed, yielding amplitude and phase images as described in Chap. 2. Note that this heterodyne technique uses a principle for expanding the time resolution over that given by the frame rate, which is similar to that of the undersampling technique described in Sect. 2.4. Resistive and Peltier heating could clearly be distinguished from each other by their different modulation frequency and their different signal dependence on the driving voltage amplitude (resistive: square dependence; Peltier: linear dependence). The spatial resolution of this system was below 1 μm, but the temperature resolution was obviously only of the order of 0.1–1 K. The spatial resolution of thermoreflectance investigations has been improved to below 50 nm by Goodson and Ashegi [71] by illuminating the sample with a scanning near-field optical microscope (SNOM). However, in this SNOM technique the illuminating light power was limited to some nW, and only a very small fraction of the reflected light could be detected. Therefore typical detected temperature modulation amplitudes were of the order of 50 K, hence the sensitivity of this technique was obviously only of the order of a few Kelvin. The general advantage of photoreflectance methods over the IR detection is its lower price and the possibility to attain a sub-micron spatial resolution. However, photoreflectance needs a well-reflecting plane surface. It can hardly be used e.g. for investigating textured solar cells or 3-D structures. Moreover, the temperature resolution of typically 0.1 K restricts its use for device testing to medium and high-power devices. There are some other techniques related to thermoreflectance such as off-axis thermoelastic deformation measurements (Opsal et al. [72]), optical beam deflection with striking incidence using the mirage effect (Murphy and Aamodt [73]), or photothermal displacement interferometry (Suemune et al. [74]). According to the knowledge of the authors, however, these techniques have been developed and used primarily for investigating thermal diffusion phenomena on layered structures rather than for imaging heat sources in electronic devices. Some of these techniques are only practicable for flat surfaces and cannot be used, e.g., for texturized solar cells or ICs with a surface topography.

Besides IR thermography and photothermal techniques, there are three other camera-based thermography techniques based on visible light microscopy and two based on near IR microscopy, which are widely used in electronic device testing and failure analysis. These are thermal mapping using nematic or thermochromic liquid crystals, fluorescent microthermal imaging (FMI), Moiré imaging, and Schlieren imaging. Nematic liquid crystals show a phase transition between liquid and liquid crystalline, which may be as sharp as 0.1 K. If a sample, covered with a thin liquid crystal layer, is illuminated with polarized light and imaged through a crossed polarizer, it appears dark above the phase transition temperature and bright below that temperature. By carefully adjusting the sample temperature just below the transition temperature, only the regions around local heat sources may appear dark. Within a certain temperature range of thermochromic liquid crystals their spectral reflectivity depends on the temperature. Thus, when illuminated with white light, their colour depends on the temperature. The sensitivity limit of nematic liquid crystal investigations is about 0.1 K, but that of thermochromic ones is even worse. Both techniques are commercially available [75]. Note that working with liquid crystals is somewhat tricky and requires a lot of experience. Especially for investigating ICs it is hard

to guarantee a complete and homogeneous wetting of the surface. This holds especially near wire bonds, since owing to capillary forces, the liquid tends to crawl up the bond wires. Recently, an interesting new technique has been introduced where micron-sized cholestric (thermochromic) liquid crystals droplet are dispersed in a polymer foil, which is loosely attached to the sample [76]. This technique has the advantage that it does not pollute the sample. However, due to the thickness of the polymer films of several 100 μm this method is only applicable to large plane samples such as solar cells, but not to ICs. Based on this principle, a "Shuntometer" for imaging strong shunts in solar cells under reverse bias with a spatial resolution of some millimeters is available [77].

Fluorescent Microthermal Imaging (FMI) investigations are based on the strong temperature dependence of certain organic dyes. A thin dye layer is applied to the surface under investigation and homogeneously illuminated by UV light. Near local heat sources, the luminescence is quenched. Hot spots are revealed by subtracting or dividing two luminescence images, with the heat sources switched on and off. Using a slow-scan CCD camera with 40 s total exposure time and an image of effectively 50×50 points, Kolodner and Tyson achieved a thermal resolution of 10 mK at a spatial resolution of 15 μm [41]. These data allow one to calculate the pixel-related system noise density, defined in (2.31) of Sect. 2.6 to be $N_{\mathrm{sys}} = 1.26\,\mathrm{mK}\sqrt{\mathrm{s}}$ for this measurement. FMI can easily be realized with a fluorescence microscope and a sensitive CCD camera (usually cooled slow-scan CCD cameras are used) and is widely used in semiconductor research. Although especially FMI has established itself as a standard technique in IC testing, also its thermal resolution is not yet sufficient for imaging weak heat sources in the μW range, which may produce temperature contrasts well below 1 mK in silicon components (see Sect. 6.1). This has recently been improved by performing FMI in lock-in mode also [78, 79]. By this measure both the spatial resolution and the detection limit of FMI considerably improve. However, according to the experience of the authors, the detection limit of lock-in FMI is still about an order of magnitude worse than that of lock-in IR-thermography under comparable conditions. In [79] the name "Stabilized FMI" has been used for single phase (0°) lock-in FMI.

Another relatively simple thermography technique is Moiré thermal imaging. This technique is performed for backside imaging of integrated circuits (ICs) under non-coherent laser light illumination at about 1064 or 1400 nm. At this wavelength the silicon substrate is essentially transparent. Since the polished backside of the IC is never exactly parallel to the front plane (it may be prepared even deliberately at a certain angle to the front plane), the monochromatic illumination generates a pattern of interference fringes (so-called Moiré pattern) at the surface. If a local heat source is present, the dimensions of the sample slightly vary, leading to a lateral movement of the Moiré pattern. If the heat source is modulated and the Moiré pattern is lock-in correlated, the local amplitude signal is a measure of the locally dissipated power density. This technique was called "Moiré Stabilized Thermal Imaging" [79]. The sensitivity of this technique is about a factor of 5 worse than that of lock-in FMI and the spatial resolution is only in the order of the sample thickness. Nevertheless, it

allows the localization of stronger local heat sources and the identification of entire array blocks with low power consumption [79].

Schlieren thermal mapping uses the angular deviation of a near-IR beam (1060 nm) caused by local heating [80]. This investigation is usually performed from the back side of an IC. Topside Schlieren imaging requires a suitable coating. For the OptoMetrix Schlieren thermal mapper a spatial resolution below 1 μm and a thermal resolution better than 10 mK have been reported [80].

It should be noted that two other very successful optical imaging technique for IC testing are photon emission microscopy in the visible and near IR range and thermal laser stimulation techniques. Light emission microscopy is also commercially available e.g. from Hamamatsu [20]. With this technique it is possible to visualize internal breakdowns in the semiconductor components due to electrostatic discharge (ESD) failure, leakage, hot carrier generation, and latch-up effects. However, purely resistive heat sources such as short circuits in metallizations usually cannot be imaged. Also defects below metallization layers remain invisible in emission microscopy, unless it is performed upside down by looking "through the chip". Moreover, the light emission dramatically drops with decreasing supply voltage of the components, since this emission is based on high field phenomena. Hence, highly sensitive microscopic lock-in thermography may reveal more phenomena than emission microscopy does, but it does not have the spatial and temporal resolution of emission microscopy. Therefore, microscopic lock-in thermography may be at least a valuable supplement to photon emission microscopy. For investigating components having low supply voltages, where emission microscopy more and more fails, lock-in thermography may be substituted for emission microscopy for IC testing.

Thermal laser stimulation techniques like OBIRCH (Optical Beam Induced Resistance Change [81]) and TIVA (Thermally Induced Voltage Analysis [82]) are based on the temperature coefficient of any kind of leakage current in an IC. Hence, the supply current or the supply voltage (at constant current) of an IC is monitored, and the active region is scanned by a focused laser beam of up to 100 mW power. In order to avoid optical absorption, a wavelength of about 1360 nm is used, which also allows to perform this investigation from the back side of the sample. As soon as the laser beam hits a leakage site, the detected current or voltage signal changes, which allows one to image these leakage sites. OBIRCH and TIVA can also be used in lock-in mode, which improves their detection sensitivity [83, 84].

Note that (lock-in) thermography and thermal laser stimulation techniques are imaging the same type of defects. In both the cases a resistance-limited current of a certain magnitude, which also generates a certain local heating power, can be imaged. If a current flows through a low-ohmic line, it can be imaged neither by lock-in thermography nor by laser stimulation techniques. Systematic differences of the detectability of different defects by lock-in thermography and laser stimulation techniques will be discussed at the end of Sect. 6.1.

Infrared (IR) thermography can be applied as a serially scanning measurement and using an IR camera. The first commercial system for thermo-elastic imaging (vibrothermography) was a serially measuring system, where a slow mirror scanner

was used to scan the image point by point during the whole investigation (SPATE 8000/9000 [7]). The minimum spatial resolution was about 0.5 mm. The IR light was detected by a sensitive IR detector, and a commercial two-channel analog lock-in amplifier (SPATE 9000) was used to perform the lock-in correlation. The output of the lock-in amplifier was digitized and processed to obtain both the amplitude and phase images. The minimum necessary measurement time for imaging a 100×100 pixel field was 1000 s (17 min) assuming the use of only one 10 Hz-period per image point, resulting in a thermal resolution of the order of 0.1 K. In a real thermomechanical measurement, however, averaging over many periods is necessary to obtain a satisfactory signal-to-noise ratio, hence real measurement times of this system are many hours. Thus, for the SPATE technique, a pixel-related system noise density of the order of $10\,\mathrm{mK}\sqrt{\mathrm{s}}$ according to (2.31) can be estimated. Breitenstein et al. [85] also performed serial lock-in thermography on leakage currents of solar cells, using a mechanical x-y drive with a spatial resolution of 0.1 mm and a single liquid-nitrogen cooled MCT detector equipped with germanium optics. With a lock-in frequency of 3 Hz and averaging over 5 periods per position, the measurement time of 100×100 pixel per image was 5.5 hrs and the noise level was about 2 mK. This corresponds to a system noise density of about $2.8\,\mathrm{mK}\sqrt{\mathrm{s}}$. The improved sensitivity compared to the SPATE system was essentially due to the larger numerical aperture provided by the IR optics used in the latter investigation. Fletcher et al. [86, 87] have introduced a SNOM-type serially scanning IR microscope, which also might be used for electronic device testing. Using a microfabricated solid immersion lens with a numerical aperture of 2.5, they attained a focused spot size of $\Lambda/5$ for $\Lambda = 9.3\,\mu\mathrm{m}$ IR light. However, no data as to the thermal resolution have been cited.

The classical technique of the thermographic inspection of electronic devices is to use an infrared (IR) camera as described in Sect. 2.1. Standard (steady-state) IR thermography is the method of choice to detect, for instance, critical hot components within extended electronic equipments (ICs, line regulators, etc.), which may limit the long-term reliability of these equipments [88]. But also within single components thermography can be used to detect "hot spots", which mark the location of leakage currents. Thus, Simo and Martinuzzi [89] have imaged hot spots in heavily dislocated regions of multicrystalline silicon solar cells. Although their pixel resolution was well below 1 mm, their real spatial resolution was only in the range of several mm due to the large lateral heat conductivity of silicon. Also their sensitivity of about 0.1 K did not suffice to detect hot spots under forward bias conditions. Only after applying >10 V reverse bias, leakage sites were detected. Kaminski et al. [30] have averaged 1000 images of silicon solar cells under forward bias and have subtracted the average over 1000 images without applied bias, thereby reducing the statistical noise and subtracting the topography contrast in the thermograms. Using this static averaging and topography subtraction technique, they improved their thermal sensitivity to below 10 mK, which was sufficient to image strong shunts under forward bias conditions. However, also their images showed a strong degradation of the effective spatial resolution due to lateral heat spreading. The same holds for the very low frequency (0.05 Hz) lock-in thermography approach of Rappich et al. [90]. Gross et al. [9] thermographically imaged shunts at interconnects of thin-film

solar cells also under forward bias conditions using a PtSi FPA camera with a spatial resolution well below 100 μm. Note, however, that these solar cells are made on glass substrates, which show a weak heat conductivity. Thus, here the thermal contrasts are considerably stronger and better localized than in silicon components. For investigating integrated circuits (ICs) commercial IR microscopes are available, for instance at Hamamatsu [20] and Quantumfocus Instruments [91]. The latter system also provides emissivity correction (see Sect. 5.3) as well as time resolved measurements for a bandwidth of 250 kHz. However, the temperature resolution of both systems is only 0.1 K, since both do not yet use any signal averaging techniques. Hence, the application of these systems is restricted to medium and high-power devices, which produce surface temperature contrasts well above 0.1 K. Recently, Hamamatsu has launched the new "THEMOS mini" system, which also provides real two-phase lock-in thermography (see Sect. 3.2). Note that, for investigating microscopic heat sources in ICs, usually 3-dimensional heat diffusion has to be considered since these heat sources have small sizes. Therefore, even if a low lock-in frequency or even steady-state imaging is used, the spatial resolution for investigating ICs may be significantly better than for investigating solar cells (see Chap. 4).

Lock-in thermography in the sense described in Sect. 2.3 was proposed already by Carlomagno et al. [92], but it could not be realized yet at that time. The first camera-based lock-in thermography realization was described by Beaudoin et al. [93]. Here the lock-in correlation occurred off-line, hence after the measurement, on saved images of only 4 measured lock-in periods. According to the knowledge of the authors, Kuo et al. [4] have published first details of an IR-camera based lock-in thermography system with on-line image correlation. In this system, two commercial digital graphics processors in a VME bus workstation are used for digitizing and processing the output of a mirror scanner IR camera. The camera was running in interlaced mode at a full frame rate of 30 Hz. A fixed lock-in frequency of 15 Hz was chosen, always two successive frames were subtracted from each other, and the difference was summed up in the video processor boards. This procedure was performed separately with the two half-frames in the two image processors. Since the two half-frames are time separated from each other by 1/60 s, corresponding to a phase difference of 90° for $f_{\text{lock-in}} = 15$ Hz, the processed results of the two half-frames correspond to the in-phase (0°) and the quadrature (90°) signal. Hence, this procedure is equivalent to the 4-point correlation procedure described in Sect. 2.2. In fact, this was the first IR camera-based lock-in thermography system employing the two-phase on-line image correlation. This system was used for imaging current-induced heating in thin copper films evaporated on a Kapton foil forming a resistive microbridge. Hence, this was also the first application of lock-in thermography to electronic device testing. No sensitivity values have explicitly been cited, but the expected $1/\sqrt{t_{\text{acq}}}$ dependence of the noise voltage has been demonstrated.

The first commercial IR-camera based lock-in thermography system was a lock-in option to the AGEMA Thermovision 900 mirror scanner thermocamera, which was developed on the basis of the work by Busse et al. [94,95]. This camera worked in the long-range with a frame rate of 15 Hz at a resolution of 272 × 136 pixels. The lock-in correlation occurred off-line in this system, hence all frames of

a measurement were captured and stored in the computer. After the measurement the correlation was performed with the "4-bucket" method (see Sect. 2.2). The maximum possible number of stored frames was 1000, corresponding to a maximum possible data acquisition time of roughly one minute. After this time, the amplitude noise level of this system was of the order of 15 mK [85]. According to (2.31) this corresponds to a system noise density of $N_{sys} = 0.63\,\mathrm{mK}\sqrt{\mathrm{s}}$. Note, however, that this noise density does not yet take into account the off-line data evaluation time, which was even longer than the actual measurement time for this system. This system, which was a synchronously working system in the sense discussed in Fig. 2.7, was used primarily for non-destructive testing purposes, but also electronic devices have been tested [96]. It is no longer available. Meanwhile, AGEMA have moved to FLIR systems [21]. An off-line working lock-in thermography system (IrNDT-LockIn), which is similar to the AGEMA one but based on a special multifunctional frame grabber board and equipped with additional analytic functions, is available at Automation Technology [22]. Now this company is also offering a system implying on-line correlation (see Sect. 3.2).

The first commercial lock-in thermography system based on a highly sensitive focal plane array camera and on the on-line sin/cos correlation was the ALTAIR LI system developed by CEDIP [17]. This originally French company is now also part of FLIR systems [21]. The frame capturing and lock-in correlation are performed by a special frame grabber board and a DSP (digital signal processor) board, which were both developed by CEDIP. This system was designed for the asynchronous correlation, since it was developed for thermomechanic (vibrothermography) investigations. As has been discussed in Sect. 2.4, the asynchronous correlation has the advantage that without any modifications the lock-in frequency may be higher than the frame rate (asynchronous undersampling). However, it has the disadvantage that phase jitter and an incomplete number of acquired lock-in periods may induce additional noise. Therefore, the DSP software of the CEDIP system was designed to subtract the mean level of the signal before the correlation procedure, which reduces this additional noise. On the other hand, this subtraction introduces another numerical step in the on-line correlation procedure, which limits the processing speed of the DSP. The first system of this type worked with a 128×128 pixel resolution, but meanwhile systems offering 320×256 pixels are available both for the long range and for the mid range. For the latter system, a noise level of 1 mK peak-peak was reported after an acquisition time of 200 s [17]. According to (2.31), these data correspond to a pixel-related system noise density of about $51\,\mu\mathrm{K}\sqrt{\mathrm{s}}$, which is an improvement by a factor of 12 compared to the Agema 900 system. A similar system with a similar technical concept for different resolutions is also available from Stress Photonics [18]. Their presently highest resolution version DeltaTherm 1550 has also got a spatial resolution of 320×256 pixels, reaching a full-field thermal resolution of 2 mK after 30 s of acquisition time, corresponding to a noise density of $38\,\mu\mathrm{K}\sqrt{\mathrm{s}}$.

Since 1992 shunting phenomena in solar cells have been investigated at the Max Planck Institute of Microstructure Physics in Halle (Germany). Right from the beginning, thermal methods have been considered to detect local shunts, but the temperature sensitivity of conventional IR cameras turned out to be clearly

insufficient for this purpose. Note that a solar cell in operation is forward-biased to about 0.5 V (see Sect. 6.2). In order to detect local sites of increased forward current, which are usually called "shunts" even if they are no real short circuits, a bias of only 0.5 V has to be applied to simulate real operation conditions. Shunt currents below 1 mA, already interesting to investigate, produce a local heating in the 100 μW range, which cause a local heating in the range of 100 μK (see Sect. 4.3). The first system allowing to image temperature modulations below 100 μK was the Dynamic Precision Contact Thermography (DPCT), which was a serially measuring system [67]. Hence, for attaining this thermal resolution, for 100 × 100 pixels a measurement time above 5 hrs was necessary, corresponding to a system noise density of 0.082 mK$\sqrt{s}$. Since 1997, an IR camera based lock-in thermography system was being developed at MPI Halle, which was straightforwardly designed to reach an ultimate thermal sensitivity. With a 128 × 128 pixel resolution, its noise level of 0.03 mK after an acquisition time of 1000 s corresponded to a system noise density of 7 μK$\sqrt{s}$. This was also the first system to demonstrate the advantages of microscopic lock-in thermography for integrated circuit testing down to a spatial resolution of 5 μm [97]. Based on this development, Thermosensorik GmbH Erlangen has developed the commercial system TDL 384 M 'Lock-in' [19, 78]. With a resolution of 384 × 288 pixel and a noise level of 0.072 mK after an acquisition time of 1000 s (corresponding to a system noise density of 7 μK$\sqrt{s}$), this system was the highest sensitive commercial lock-in thermography system with the highest resolution at that time. This system was especially designed to meet the demands of diagnostics and failure analysis of electronic components. Meanwhile also systems implying a 256×256 pixel high speed MCT camera (TDL 256 HS) as well as implying a 640 × 512 pixel InSb detector (TDL 640 SM) are available. In the following section, the design philosophy of these systems will be compared with that of other commercially available lock-in thermography systems. Table 3.1 summarizes the major technical data of several lock-in thermography systems, of which the pixel-related system noise densities are known. For comparison, also the corresponding data of steady-state Fluorescent Microthermal Imaging (FMI) from [41] are given, which before the advent of IR-based lock-in thermography systems was the most

Table 3.1 Technical data of different lock-in thermography systems in comparison with FMI

System	Resolution (pixel)	Noise level (mK)	Acquisition time (s)	Noise density (mK$\sqrt{s}$)	Reference
SPATE 9000	100 × 100	100	1000	31	[7]
Agema 900	272 × 137	15	66	0.63	[85]
CEDIP	320 × 240	1	200	0.051	[17]
DeltaTherm 1550	320 × 256	2	30	0.038	[18]
DPCT	100 × 100	0.058	20,000	0.092	[68]
MPI Halle	128 × 128	0.03	1000	0.007	[97]
TDL 384 M	384 × 288	0.072	1000	0.007	[78]
TDL 640 SM	640 × 512	0.092	1000	0.005	this work
TDL 256 HS	256 × 256	0.2	0.9	0.0008	[98]
FMI (steady-state)	50 × 50	10	40	1.26	[41]

sensitive thermal technique of investigating electronic devices. The exceptionally good pixel-related noise density of the TDL 256 HS system is due to two factors: (1) The detector works in "integrate-while-read" mode and the readout circuit is so fast that the camera is integrating photons for more than 80% of the acquisition time. (2) The detector pixels are with $40 \times 40\,\mu m$ exceptionally large, hence they are able to collect many photons. On the other hand, the latter property makes this camera less appropriate for microscopic failure analysis on ICs, since here a very high magnification microscope objective would be necessary to obtain a good spatial resolution. However, for microscopic imaging, the brightness of the image inherently reduces with the square of the magnification factor (see Sect. 3.4), hence the advantage of good sensitivity will get lost. It is obvious that the sensitivity of the most sensitive IR-camera based lock-in thermography systems compared to FMI is improved by a factor of 250! This demonstrates the enormous gain in information that can be expected if FMI is replaced by IR lock-in thermography.

3.2 Commercial Lock-in Thermography Systems

In this section the design philosophies of different commercial lock-in thermography systems will be compared and related to their different application fields. It was already mentioned in the earlier section that the first commercial lock-in thermography systems were introduced by AGEMA and CEDIP. The AGEMA system was designed for performing photothermal investigations, hence to investigate the temperature modulation of a surface under the influence of modulated irradiation of light. If there are sub-surface defects in the material, the surface temperature modulation is locally disturbed, which allows to detect such defects [2]. The system allowed to generate a programmable analog waveform synchroneous to the lock-in correlation, which enabled the user to generate a sin-shaped light intensity modulation. As mentioned before, the system was operating synchroneously, hence the lock-in trigger was derived from the frame trigger of the free-running IR camera, and 4-bucket correlation was performed off-line after all images were stored. This has limited the maximum number of evaluated frames to 1000. This system is not available anymore, but several other lock-in thermography systems being specialized to NDT have followed the tradition of this development, like that of Automation Technology [22] and edevis [23]. They are all now based on modern FPA thermocameras, they can be used both for lock-in and pulse thermography, and they can apply different stimulation means like halogen lamps, flash lamps, laser, ultrasonic, eddy current, or mechanical excitation. The correlation type may be synchroneous or asynchroneous at choice, and the correlation may be performed on-line or off-line. However, these systems are not primarily designed for the investigation of electronic components. Of course, here also it is no problem to use an externally controlled power supply as a stimulation mean for applying a pulsed bias to an electronic device. However, e.g. reading back the flowing current, which is a decisive parameter to be measured in electronic device testing, is generally not implemented in the software. Generally, NDT systems are meant for macroscopic investigations,

hence microscope objectives are usually not provided. The use of solid immersion lenses for improving the spatial resolution (see Sect. 3.4) is not even meaningful if other excitation means than internal electric heating are applied. The systems of Automation Technology are now also offered by moviTHERM [28].

The CEDIP Altair-LI system, which is still available from FLIR [21], was the first commercial lock-in thermography system with two-phase on-line lock-in correlation. It was designed especially for thermoelastic investigations. A similar system, also specialized to thermoelastic investigations, is available by StressPhotonics [18]. Here a mechanical device is stressed periodically from compression to expansion in a special deformation machine. Similar to a compressed and expanded gas, in regions of strain, the solid material gets periodically heated and cooled, which is the so-called thermoelastic effect [2]. Hence, lock-in thermography allows to image the local strain rate in the device quantitatively and, for higher deformation amplitudes, also plastic deformation regions. Since, at least in the early days of these investigations, the deformation machines were freely running, the CEDIP system was designed consequently for asynchroneous correlation. Hence, the IR camera is also freely running at its own frame rate and the deformation machine (or any other signal generation means) has to provide a TTL or analog trigger signal which is synchroneous to the expected T-modulation. As described in Sect. 2.5, the system detects in each period the phase of the modulation trigger with respect to the periods of the IR camera and selects the correct values of the correlation vectors from a look-up table. Since for asynchroneous correlation, especially for a small number of lock-in periods, the sum of all weighting factors may be not exactly zero, the d.c. value of the IR-images is generally subtracted before correlation for avoiding additional noise contributions [29]. This system easily allows to operate in the (asynchroneous) undersampling mode, hence the modulation frequency is allowed to be above the frame rate of the camera. However, it has to be avoided to use "forbidden" frequencies (multiples of the Nyquist frequency) as well as, if the excitation contains higher harmonics, aliasing collisions (see Sect. 2.5). In the CEDIP Altair system, the IR camera is connected with a special hardware box (embedded into the camera itself in the newest version), which contains a frame grabber and a separate Digital Signal Processor (DSP) system. The actual lock-in correlation procedure of the image data is performed by this DSP system and only the final results are transmitted to the host PC where the Altair-LI software is running. This philosophy avoids the problems of processing fast continuous data streams, which have been inherent to earlier Windows versions running on computers about 10 years ago. The actual CEDIP Altair-LI software is specialized to stress measurement applications and allows processing periodic and non-periodic (random) mechanical loading. However, CEDIP (now FLIR) offers a developer-kit based on C^{++} under Windows, which allows the user to write his own lock-in thermography application. The NDT systems of Automation Technology and edevis as well as the AescuSoft system (see below) were originally developed based on the CEDIP developer kit.

The first commercial lock-in thermography system, which was consequently specialized to functional diagnostics of electronic components, was the TDL 384 M 'Lock-in' system by Thermosensorik [19] introduced in 2000. Here TDL stands

Fig. 3.2 The Thermosensorik TDL 640 SM 'Lock-in' system

for "Thermosensoric Defect Localization", 384 is the x-resolution in pixels (meanwhile higher resolutions are available), and M means "midwave". This system was developed using the experiences made at the construction of the DSP-based lock-in thermography system at Max Planck Institute in Halle, Germany [97]. In its standard configuration, the camera is mounted on a stable vertical pillar, looking down with variable distance to the sample (see Fig. 3.2). By using a number of wide-angle and microscope-type IR-objectives, this construction allows to apply the system both for microscopic (IC analysis) and macroscopic (e.g. solar cell) applications. Of course, for imaging even larger objects like solar modules, the camera can be mounted horizontally also. Despite being a highly sensitive thermography system, as a lock-in system it does not need a housing. Nevertheless, a housing also implying illumination means is available. The Thermosensorik systems are not based on complete IR-cameras, which contain their own two-point calibration system and can be operated also without a computer. Instead, only the basic camera modules are contained in the camera housing and the two-point calibration and bad pixel correction are

performed by a connected PC under Windows. Also the lock-in correlation procedure is performed under Windows by the PC and not by a separate DSP system. This is a very economic solution, but its programming is very demanding if numeric errors should be avoided. Note that Windows is internally organizing the timing of its own jobs, it is no real time system. Therefore, for this video-type application there is always the danger to loose one or a few images for the correlation. It was explained in Sects. 2.2 and 2.5 that it is essential for the lock-in correlation procedure that the total sum of all correlation coefficients is zero, assuming that all measurement values are present. If one image should be lost, this is equivalent to setting one correlation coefficient to zero, so their total sum is not zero anymore. If this happens, the primary lock-in thermography images (0°- and −90°-image) contain residues of the topography signal. Hence, if single images are lost for the correlation, the perfect d.c.-suppression property of the synchroneous lock-in correlation procedure gets lost. By applying special proprietary means this can be avoided in the Thermosensorik systems also under Microsoft Windows operation. Since the heat generation in semiconductor devices can easily be controlled externally by applying appropriate bias signals, the Thermosensorik systems are generally applying synchroneous correlation, hence the lock-in trigger is derived from the frame trigger of the camera by a frequency divider. As it was discussed in Sect. 2.5, this operation mode ensures optimum d.c.-suppression and minimum noise, but it does not enable to expand the lock-in frequency range above $f_{\mathrm{frame}}/4$ by using undersampling. Undersampling is available also for these systems as a special option, which uses external IR camera triggering (see Sect. 2.5). As the user surface of present Thermosensorik lock-in thermography systems shows (Fig. 3.3), the application of a pulsed bias is integral part of the system (see “Voltage 2”, bottom

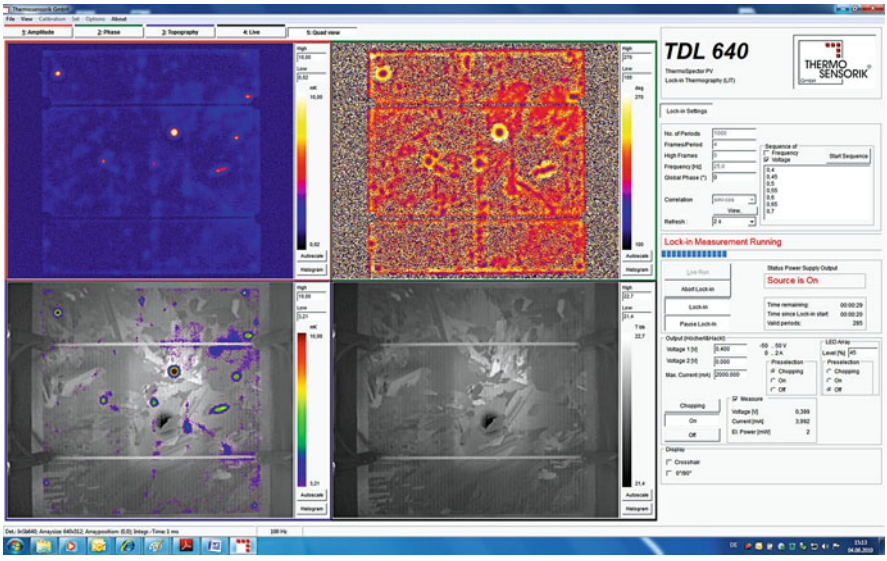

Fig. 3.3 User surface of the Thermosensorik lock-in thermography systems

right region). Depending on the intended application (IC failure analysis, solar cell research, CDI/ILM, solar module investigations, NDT), the system may work with different types of power supplies or other signal generation means such as LED arrays or lasers, which may be controlled by a TTL trigger. For modulation, the sample bias may be switched between on and off (square wave modulation, 100% degree of modulation), or a constant bias may be square-modulated by a certain amount without switching the bias completely off, which is often necessary for IC failure analysis. The bias in the "off" phase can be set in the "Voltage 1" field. Sinusoidal bias modulation is also provided in this software. However, for testing electronic components it is not useful (see Sect. 2.5). An important feature is that the real bias and current values, which are always read by the power supply directly at the sample by using a 4-wire connection at the beginning of each measurement, are displayed in addition to the set voltage and current limit and the polarity settings (see bottom right corner in Fig. 3.3). This display is essential, since the applied voltage and the flowing current are two dominant experimental parameters in electronic device testing. Only by this reading, the operator is informed what really happens with the device, and unintended opens or shorts in the current path to the device or overloading can easily be recognized. The alternative Chopping "ON" and "OFF" buttons at the bottom allow to apply the bias (pulses) to the sample already before the lock-in measurement starts. This allows to prevent the initial heating-up phase at the beginning of a lock-in measurement, see Sect. 4.1. Alternatively, there is the option to include the temperature drift compensation according to Sect. 4.2. The Thermosensorik systems also imply a quick current-voltage (I-V) measurement option for easily finding out the optimum bias setting for the lock-in measurement. The user surface shown in Fig. 3.3 is widely self-explaining and abandons extra windows for performing the lock-in measurement. In the LockIn-Settings the number of frames per period and the resulting lock-in frequency (which can be set also explicitely), the number of lock-in periods to sum up (leading to a certain acquisition time, which is indicated under "time remaining"), the global phase setting, the correlation type (sin/-cos as standard, also sin/cos and square/triangle is possible), and the image refresh time. The global phase setting allows one to correct for any unintended delays between the lock-in pulse-trigger and the photon detection periods of the IR camera. Note that according to Sect. 2.2 (2.10) the lock-in evaluation process assumes that the photon detection period of the first image evaluated in each lock-in period is centered exactly at $t = 0$, where the heating power switches on (cf. also Fig. 2.6 in Sect. 2.3). In reality, due to inevitable delays in the camera control circuits, this is usually not the case. Hence, especially for high lock-in frequencies, where such delays become important, the calculated 0°- and the −90°-image according to (2.4) and (2.10) are not exactly these images but contain a certain phase error. This systematic phase error, as well as additional phase errors caused e.g. by using a black paint on the sample for homogenizing its emissivity, can be corrected by the global phase setting. By applying (2.9) from Sect. 2.2, the system corrects the phase of the results so that the displayed image A is exactly the 0°-image and the image B is exactly the −90°-image. How to find the correct value for the global phase setting will be described in Sect. 5.1. After a lock-in

measurement, the Thermosensorik systems are storing and saving only the topography image and the two primary lock-in images measured by applying (2.4) and (2.10) as floating point data arrays. From the latter, all possible lock-in images, such as the (phase-corrected) 0°- and −90°-image (here called image A and B), the amplitude image, and the phase image, are generated for display. By checking the "0°/− 90°" box, instead of the phase image the 0°/− 90°-image can be displayed (see Sects. 4.5 and 5.1). Four images (e.g. amplitude, phase, overlay of topography and amplitude, and live image) are displayed in full resolution or one of the four images in 2-fold magnification. In the "View" menu it can be selected whether the A or B images (0° and −90° images) or the amplitude and phase (or 0°/−90°) images are displayed. The images can also be zoomed and different colour palettes can be chosen. The scaling means beside the images allow to scale all images separately, which can be done either manually, by using a histogram, or automatically. Either the amplitude or the phase image (or alternatively image A or B or the 0°/−90° image) may be superimposed to the topography image, which is called here "Overlay". In the "Calibration" menu the 2-point calibration for different imaging conditions can be performed and administrated. Alternatively, in any "life" mode also a quick possibility to perform this calibration e.g. by using the lab temperature (objective cap) and the temperature of the palm of the hand is provided. In the "Set" menu the frame mode of the camera (full frame or different sub-frame modes), the image integration time, and different other camera parameters may be set. The four bottoms right of the images allow to choose the life imaging mode of the camera, to start or pause a lock-in measurement, and to abort it. Aborting a measurement is equivalent to finishing a measurement after the programmed time, hence the lock-in data gained up to this moment are ready for display. The field in the rightmost upper part of the user surface allows to define a number of lock-in frequencies or voltages, which are used in a batch measurement. Hence, by pressing "Start Sequence" a number of lock-in measurements with different parameters as defined in the parameter list are performed and saved as different files with the parameter values appended to the file name. As a typical noise measurement, Fig. 3.4 shows the amplitude noise of the system as a function of acquisition time by using a 640 × 512 pixel midwave InSb (indium antimonide) camera. The measurements were performed at a full frame rate of 100 Hz, using a lock-in frequency of 10 Hz (10 frames per period) and a frame integration time of 0.7 ms. For this measurement, the IR-objective was closed by the black plastic lens cap, hence the object was a black body at room temperature (about 25°C), and the amplitude signal was averaged over a representative area. The data in Fig. 3.3 can be fitted by $A_{\mathrm{noise}} = 2.9\,\mathrm{mK}/\sqrt{t_{\mathrm{acq}}}$. Hence, according to (2.31) in Sect. 2.5, this corresponds to a pixel-related system noise density of $0.005\,\mathrm{mK}\sqrt{\mathrm{s}}$, which was also included in Table 3.1 in Sect. 3.1. Figure 3.5 shows the dependence of the noise density of this camera on the lock-in frequency for a fixed acquisition time. It turns out that the noise somewhat increases towards low frequencies. This points to a certain $1/f$ noise contribution in the noise density of the camera, which is typical for electronic noise.

Two other companies, InfraTec [25] and AescuSoft [24], are offering lock-in thermography systems, which are specialized for illuminated lock-in thermography

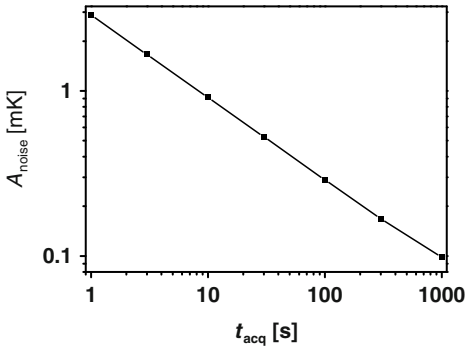

Fig. 3.4 Results of noise measurements of the Thermosensorik TDL 640 SM 'Lock-in' system

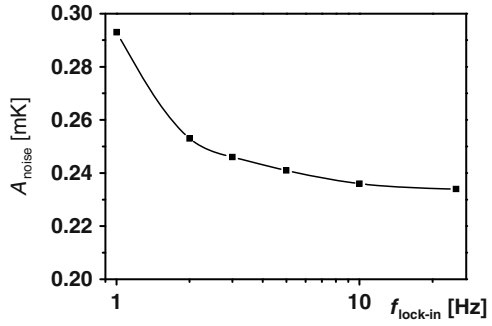

Fig. 3.5 Measured frequency dependence of the noise amplitude

(ILIT) on solar cells (see Sects. 2.6 and 6.2) and on free carrier detection on solar materials (see Sects. 2.9, 3.5, and 6.4). The InfraTec system is based on the developments of University of Konstanz, Germany [14]. They developed a technique called "LimoLIT" ("light-modulated lock-in thermography", which was later called "Voc-ILIT" [16], see Sect. 6.2), where the solar cell is periodically irradiated by an infrared luminescence diode (LED) array (see Sect. 3.3). In order to provide the optimal adaption to the properties of the solar cell material, the changeable LED modules can be selected from a variety with alternative wavelengths (IR, VIS). Alternatively, the InfraTec system supports - additional to the non-contact measurement - also the voltage modulated "VomoLIT" or "DLIT" mode, where the solar cell or module is excited by electrical current. In the InfraTec systems, both the IR camera and the lock-in excitation are triggered by the same clock generator via two independently programmable frequency dividers, as it has been described in Sect. 2.5. However, undersampling is not possible until now. As for other on-line correlating systems, the control software emphasizes continuously visual presentation of the results. Hence, all calculated images as topography, amplitude, phase and single phase image (additional to 0° and 90° also with random selectable angle) are shown and refreshed periodically from begin of the measurement on. A certain

limitation is that the power supply for DLIT uses only 2-wire connection, hence for higher currents the bias reading is inaccurate.

The AescuSoft lock-in thermography system [24] is based on developments of Fraunhofer Institute of Solar Energy Systems (ISE) in Freiburg, Germany [13, 15, 53] and is based on the CEDIP developer kit [17, 21]. The camera and excitation triggering occurs similar to that of the InfraTec systems, hence, the frame rate of the camera can be chosen, synchroneous correlation is used, and undersampling is possible. The specialty of this system is the use of an infrared semiconductor power laser for illuminating the sample. By using a special beam expansion optics, an optical power of up to 110 W can be distributed homogeneously over an are of up to $220 \times 220\,\mathrm{mm}^2$ (see Sect. 3.3). This system is preferentially intended for illuminated lock-in thermography (ILIT) on solar cells and for free carrier detection in solar materials (see Sect. 2.9). Lock-in thermography with electrical excitation is possible as well by using an external power supply. However, the really measured voltage and current values are not brought to the user surface. The basic construction of both systems is made for macroscopic investigations of solar cells and solar materials. Hence, these systems cannot be used for IC failure analysis, where homogeneous light irradiation is not helpful anyway.

Since 2004, FA Instruments, San Jose, CA, USA [26] is offering systems called "Moire Stabilized Thermal Imaging" and "Stabilized FMI" (fluorescent microthermal imaging) for IC failure analysis [79]. Also, "Stabilized" infrared thermal imaging is available in the near IR, midwave, and in the longwave range. The name "Stabilized" is another name for single-phase (e.g. 0°) lock-in square-wave image correlation. It means that here the thermal image establishes already after one lock-in period, whereas for steady-state thermal measurements it may take seconds to minutes till a temperature distribution is stable. Taking the absolute value of the result displays both phases but at the expense of the polarity of the signal. Since the FMI film fades under UV illumination, this time saving is important for sensitivity with up to a factor of 2 improvement in sensitivity per unit time, since the phase information is foregone with single-phase lock-in. The Moire effect relies on interference fringes, which appear under monochromatic illumination at the backside inspection of ICs in the near infrared region, where the silicon material is transparent. If there are local modulated heat sources in the active region, these fringes move laterally as a result of local strain, which can be made visible by lock-in correlation of the IR images. Since Moiré does not fade with time, long acquisition times are possible. It had been already mentioned in Sect. 3.1 that performing fluorescent microthermal imaging (FMI) in lock-in or stabilized modes clearly improves the sensitivity and the effective spatial resolution over traditional background subtract techniques. Since, at least until now, the "Stabilized" thermal methods of FA Instruments comprise only single-phase correlation, a phase image cannot be displayed yet and would be beneficial especially for the Moiré technique to discriminate the thermal signal from the combined background signal seen in the amplitude signal. However, the timing relationship between the bias and the frame capture is manually adjustable to optimize this method (fixed phase adjustment).

In 2005, part of the staff of Thermosensorik has founded a new company called "IRCAM" [27]. Besides manufacturing infrared cameras and systems, IRCAM also offers a software package "IRCAM Works" for scientific and industrial applications, which also contains a functional extension "Lock-in for Works". Similar to the CEDIP system, this system is especially appropriate for thermal stress analysis (TSA) applications. By using the proprietary MIO-interface of IRCAM, both synchroneous and asynchroneous correlation can be applied at any frequency and very compact lock-in thermography systems can be built, even by using a laptop computer.

Since 2007 also Hamamatsu [20] is offering lock-in thermography as an option to their "THEMOS" systems implying a 320×240 pixel midwave InSb camera. The "Themos 1000" and "Themos mini" systems are primarily optimized for microscopic IC analysis (largest object size, which can be imaged in microscopic configuration, is 3×4 cm); however, also macro-optics can be adapted to image large areas. The complete system is mounted vibration-isolated and shielded from external radiation. As a special feature, these systems allow the users to display an "Animation," which is a time-resolved movie of the local heating over one lock-in period. The lock-in timing control is similar to that of the Thermosensorik systems, hence the camera is free running, the lock-in trigger is derived from the camera trigger, and the maximum lock-in frequency is $_{\text{frame}}/4$ (about 35 Hz). Sample biasing up to ±45 V/100 mA is integrated, also enabling a well-defined modulation depth, and internal I-V characteristic measurement and voltage/current reading are provided. This system performs two-phase correlation; hence, it allows the users to display the amplitude or the phase image. Single-phase component image like the 0°-image as well as the 0°/−90°-image can be displayed (see Sect. 5.1). The application of a solid immersion lens (SIL, see Sect. 3.4) for improving the spatial resolution is also supported.

In the basic software, the images can be displayed only in 16 colors, which cannot be changed, they are not quantitatively scaled in units of mK or degrees but rather in digits, the parameters of the IR camera and the 2-point calibration cannot be set by the operator, and no topography image is automatically stored. However, an optional quantitative analysis function is available for absolute temperature measurement. So also there is still some room for improvement. Nevertheless, the lock-in option works reliably and represents a decisive improvement of the THEMOS systems.

3.3 Illumination Systems

In this section different systems for homogeneously illuminating a macroscopic sample like a solar cell or a wafer of solar material by near-IR light, which are necessary for performing different types of illuminated lock-in thermography (ILIT) and free carrier detection will be described (see Sects. 2.9, 3.5, 6.2.2, and 6.4). We will not discuss here any focused laser stimulation techniques, which are used in IC failure analysis e.g. for OBIRCH (Optical Beam Induced Resistance Change [81])

or TIVA (Thermally Induced Voltage Analysis [82]). The optimum wavelength for exciting minority carriers in silicon is the near-IR between 840 and 960 nm, corresponding to a penetration depth in silicon between 20 and 80 μm. If the wavelength is considerably shorter than 840 nm, the increasing photon energy, compared to the energy gap of silicon, leads to a stronger thermalization heat, which is an unwanted homogeneous heat source in the different ILIT experiments, see Sect. 2.8. Moreover, for shorter wavelengths the minority carrier generation occurs very surface-near, which increases the sensitivity of these techniques to surface phenomena. If solar cells are illuminated, too short wavelengths are leading to absorption already in the emitter, what is usually not intended. If, on the other hand, the wavelength is considerably larger than 940 nm, the penetration depth may become larger than the sample thickness. This would improve the depth-homogeneity of the excitation, but then not all irradiated photons would lead to the generation of minority carriers. If larger bandgap materials like amorphous Si, CdTe, or CuInSe should be investigated, a shorter wavelength of, e.g., 700 nm has to be used.

The solar irradiation constant in middle Europe after passing the atmosphere is about 1000 W per square meter (100 mW/cm^2). This is basically white light with a colour temperature of about 6000 K, which is slightly modified by atmospheric absorption and scattering. For irradiating solar cells monochromatically under realistic conditions, the photon flux should be so, that the short circuit current density J_{sc} of the cell equals that under solar irradiation. Since the quantum efficiency of silicon solar cells is close to 1 in the wavelength range between 840 and 960 nm and the maximum possible J_{sc} is about 40 mA/cm^2, this corresponds to a photon flux of about 2.5×10^{20} photons/cm^{2}s. At a wavelength of 850 nm (1.46 eV/photon) this corresponds to an optical irradiation power of 59 mW/cm^2, which is considerably less than the solar irradiation power. Nevertheless, even this is a considerable illumination intensity, which is not trivial to generate over a typical area of a solar cell, which presently is 156×156 mm^2. For having also the possibility to work with an increased excitation intensity, many monochromatic light irradiation means are designed to illuminate at an intensity of up to 100 mW/cm^2. For these experiments, the irradiation is always assumed to be homogeneously across the whole area. Since a certain inhomogeneity of, e.g., ±10% can hardly be avoided without wasting too much of optical energy, in some experiments the local inhomogeneity of the irradiation field is mapped before and the measured results are corrected for this inhomogeneity after the measurement [53].

The first illumination system published for carrier density imaging (CDI) and later on also for ILIT was using a semiconductor laser delivering about 20 W optically at 917 nm from a glass-fiber output [13, 15, 53], see Fig. 3.6. An illumination system of this type with an output power of now up to 110 W is a part of the lock-in thermography systems of AescuSoft [24]. The laser is pulsed on/off by the lock-in system and its radiation is expanded and homogenized over the sample area by a special optics implying a microlens array. The main advantage of this solution is that here the irradiation is performed from a larger distance (≈1 m) without wasting too much optical power. However, due to the high power density of the laser, special laser safety requirements have to be fulfilled in these systems.

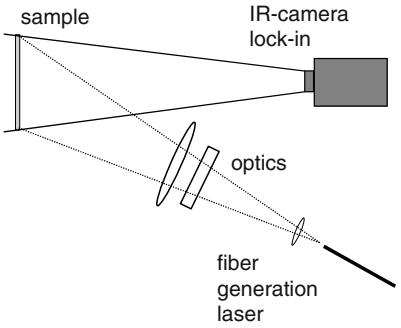

Fig. 3.6 Semiconductor laser-based illumination system of AescuSoft [24]

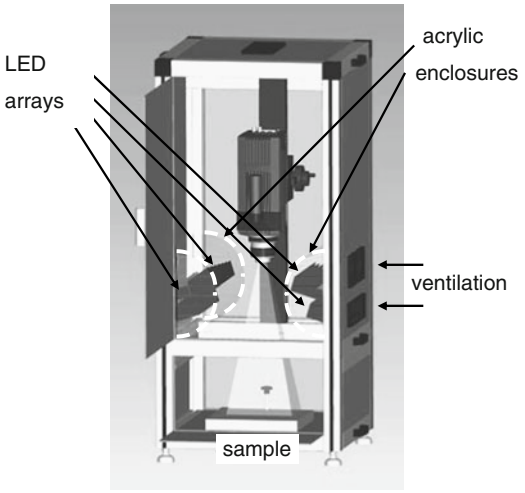

Fig. 3.7 The LED-array illumination system of InfraTec [25]

The "Limo-LIT" systems of InfraTec [25] use four LED-arrays for illumination, see Fig. 3.7. For this LED-illumination no special safety requirements have to be fulfilled. The two main problems for using LEDs for generating such a high illumination power are (1) to dissipate the heat from the LEDs and (2) to screen the sample from thermal radiation of the LEDs. Note that the LEDs are getting warm during operation. If they are operated in pulsed mode, their temperature also oscillates, leading in addition to the LED light oscillation to an oscillating thermal radiation in the wavelength range above 3 μm. The sample has to be screened from this radiation because otherwise this thermal radiation, reflected by the sample to the IR camera, would be misinterpreted as a temperature modulation of the sample. Here this screening is provided by two acrylic enclosures, which contain two LED-arrays each, irradiating downwards. Acrylic is transparent to the LED light but blocks thermal radiation. The SMD-type LEDs are mounted on heat sinks for dissipating

the generated heat. By forced cooling through special ventilation slits the heat is transported to outside the enclosures.

A certain limitation of the illumination system in Fig. 3.7 is that, due to the relatively wide irradiation angle of the LEDs of $+/-30^{\circ}$ and the big distance to the sample, an essential part of the radiation does not reach the sample area but is irradiated outside it. This loss is essentially avoided in the backside LED illumination scheme for solar cells sketched in Fig. 3.8, which was developed at Max Planck Institute (Halle). Here the "legs" of the LEDs are used in their full original length for dissipating the generated heat. The LEDs are mounted between two printed circuit boards (PCBs). In the room between these boards, where the LED legs are, an air stream flows for cooling, which is generated by a row of fans on one side of the construction. Here the solar cell is facing towards the LED array (downwards) and its back contact is directed to the IR camera (upwards). This is no serious limitation for thermal investigations since a silicon solar cell can be considered as "thermally thin", hence the temperature at its front side is essentially the same as that at its backside (see Sect. 4.1). Thermal waves easily penetrate the back contact of conventional solar cells, which is made by sintered Al-paste and even exhibits a relatively good and homogeneous IR-emissivity. Since the back contact of a solar cell is opaque to thermal radiation, an acrylic window is not necessary here. Instead, the cell is lying here on a thin transparent plastic foil (not shown in Fig. 3.8). Thin film solar cells made on a glass substrate, which are illuminated from the top rather than through the glass substrate, cannot be investigated by this setup of illumination, since this substrate is "thermally thick", hence the thermal waves generated at the active region at the bottom do not easily penetrate the glass substrate facing to the camera. Note that glass is essentially opaque to thermal radiation. On the other hand, superstrate-type thin film cells on glass like CSG-modules (crystalline silicon on glass, [99]), where the light passes the glass substrate and the IR camera may look at the active layer, can be investigated. Here the metallized surface has to be covered by an IR emitter foil, see Sect. 6.2. This setup is also less appropriate for free carrier detection (see Sect. 2.9), since these experiments require illumination from the same side where also the IR camera views. The decisive advantage of the arrangement in Fig. 3.8 is that the LEDs are positioned very close to the sample here. Thus the loss in optical

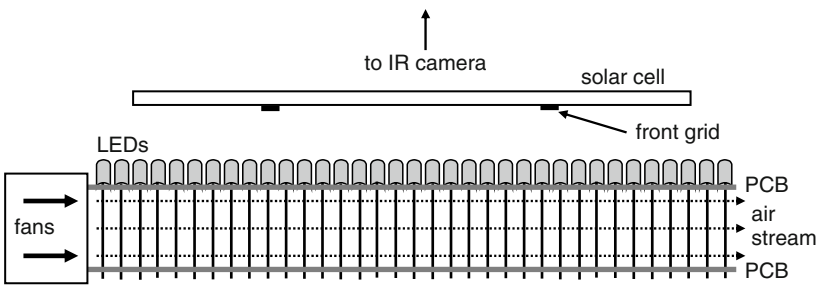

Fig. 3.8 Backside LED illumination scheme

power due to the divergence of the LED radiation is low here. This system is able to illuminate with an intensity equivalent to more than 200 mW/cm^2 (two suns).

A common problem of all LED-based illumination systems is that LEDs are traditionally low power devices. The maximum optical output power of a conventional "high power" IR-LED is about 45 mW at a current of 100 mA (SFH 4258, [100]). Hence, for generating tens of watts optical power, many hundreds of such LEDs have to be used, which may become quite cumbersome to fabricate. Illuminating even larger devices like solar modules by small LEDs becomes too expensive. However, in the last years, decisive advantages in developing high power LED modules have been made. Thus, the SFH 4740 "Ultra High Power Infrared Emitter" by Osram Opto Semiconductors generates 3.6 W optical power at 850 nm at a current of 1 A at 18 V [100]. Figure 3.9 shows an illumination system using such devices, which was also developed at Max Planck Institute (Halle). Here the IR emitter devices, which contain their own cooling plate, are mounted on a metal plate, which, on its opposite side, carries several CPU-coolers. These coolers are actually designed for cooling the central processing unit (CPU) of PCs and are working very efficiently and quietly. In the middle of the metal plate a hole for the wide-angle objective of the IR camera exists, and the IR emitters are distributed evenly around this objective. In front of the IR emitters there is an acrylic plate for

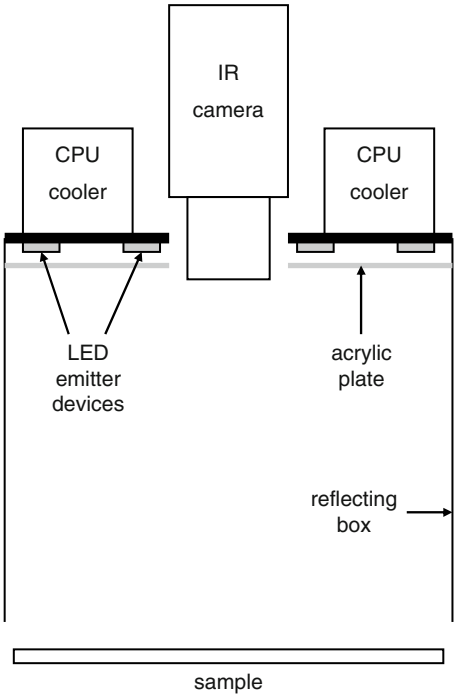

Fig. 3.9 Illumination scheme using "Ultra High Power Infrared Emitter" devices

filtering out the thermal radiation of the IR emitters. Since these emitters are radiating at a wide angle of $+/-60°$, a reflecting box is used to guide the light to the sample and to minimize optical losses. An illumination system employing 16 SFH 4740 devices and four CPU coolers was found appropriate to illuminate an area of $210 \times 210\,\mathrm{mm}^2$ homogeneously well above $60\,\mathrm{mW/cm}^2$ optical power at 850 nm, which is equivalent to sun light above $100\,\mathrm{mW/cm}^2$. The major advantages of this solution are that it is easy to assemble, that there are minimum light losses, that the illumination occurs at the same side as the IR camera views (which enables e.g. free carrier detection in emission mode, see Sect. 2.9), and that this system can easily be expanded to illuminate arbitrarily large areas. This illumination system, used for backside illumination, as well as an illumination system combining the geometry of the InfraTec system (Fig. 3.7) with lens-focused ultra high power light emitters for frontside illumination are available for different wavelengths from Thermosensorik (Erlangen) [19].

3.4 Solid Immersion Lenses

If lock-in thermography is applied for failure analysis of integrated circuits, a decisive limitation is its limited spatial resolution. Note that the decisive point is not the resolution of the lock-in images, which anyway may appear more or less blurred due to lateral heat spreading or because the actual heat source may lay at a certain depth below the surface. Even in such a case, if a heat source is point-like, the position of its center can often be estimated up to an accuracy of 1 pixel by finding the center of gravity of the blurred spot. The main problem with spatial resolution is that the operator still needs to be able to navigate on the surface of the IC! Today the layout pattern may be so small that no details can be resolved anymore with a conventional microscope objective in the mid-IR range. Therefore the challenge for improving the spatial resolution is to get a meaningful topography image, which enables an orientation on the surface. Only then local peaks in the lock-in images can be related reliably to the layout of the IC.

The resolution Δx of any optical system is physically limited by diffraction, which is governed by the wavelength λ of the radiation used for imaging. According to the so-called Sparrow Criterion [101], the optical resolution is limited to:

$$\Delta x = \frac{0.5\lambda}{n \sin(\theta)}. \tag{3.1}$$

Here θ is the half-angle of the light-cone to the objective and n is the refractive index of the medium surrounding the sample. The product $n \times \sin(\theta)$ is also called "numerical aperture" (NA). For a given magnification factor of the objective, the brightness of an image increases with the square of $\sin(\theta)$, since the number of photons reaching the detector increases with an increasing solid angle used by the objective. Even for high brilliance microscope objectives, θ can hardly be

larger than 30–45° for technical reasons, therefore $\sin(\theta)$ is at best between 0.5 and 0.7. Hence, in air ($n = 1$) the optical resolution can be only slightly better than the wavelength λ used for imaging. Therefore midwave IR cameras working in the 3–5 μm range may show a better spatial resolution than longwave cameras working at 8-12 μm. Unfortunately, for samples being close to room temperature, in the mid range the light intensity exponentially increases with wavelength, as can be seen in Fig. 2.1. So the dominant part of the light is concentrated close to 5 μm and only a negligible part appears at 3 μm. Therefore, for a good microscope objective with NA = 0.7 (+/− 45° light acceptance angle), according to (3.1) the diffraction-limited spatial resolution for $\lambda = 5\,\mu\text{m}$ is $\Delta x = 3.6\,\mu\text{m}$, independent of the magnification factor of the objective and the pitch size (pixel distance) of the detector. On the other hand, the so-called pixel resolution is the pitch size divided by the magnification factor of the objective. It may be well below this diffraction-limited optical resolution, if the magnification factor of the objective is chosen large enough. In this case all images appear naturally blurred, therefore this magnification is sometimes called an "empty" (useless) magnification.

Here some remarks to the definition of the spatial resolution should follow. Note that the term "diffraction-limited spatial resolution" refers to the minimum distance of two neighboring small spots or lines (i.e., a "line pair"), which can be separated from each other. If more than two parallel lines are used, the right line of the left line pair coincides with the left line of the right pair, hence, e.g., "288 line pairs/mm" actually means 288 lines/mm, corresponding to a line distance (center-to-center) of $X = 1/288\,\text{mm} = 3.47\,\mu\text{m}$. If such a periodic arrangement is imaged with an objective close to its resolution limit, the brightness is sine-modulated with a spatial frequency of $f = 1/X$, which is the basic spatial harmonic, see Fig. 3.10a. All higher spatial frequencies are suppressed since we have assumed that these details are below the diffraction-limited spatial resolution. The decisive point is that the spatial frequency f is only dependent on the center-to-center distance of the lines X but not on the line width w or the line distance $X - w$. Only the intensity of the basic spatial harmonic compared to higher harmonics depends on w. It is highest if $w = X/2$ holds, hence if the lines have a distance equal to their width. This is realized, e.g., in the elements of the well-known USAF resolution target, one of them sketched in Fig. 3.10b. Here three lines with a center-to-center distance X are displayed with a distance of $X/2$ in between. For 288 line pairs/mm, this distance is

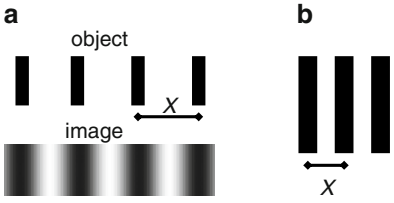

Fig. 3.10 (**a**) Line object and its image close to the resolution limit; (**b**) USAF pattern showing the spatial resolution X

about 1.74 µm. If these lines can be observed separately, the thereby proven spatial resolution is not $X/2$, but it is the center-to-center line distance X! Some authors consider the "line and space distance" $X/2$ as a measure of the resolution [102], but this overestimates the spatial resolution by a factor of 2.

Another interesting question is which magnification factor M of the lens must be used for making use of the diffraction-limited spatial resolution. One might think that a lens leading to an object pixel distance of Δx according to (3.1) should be sufficient ($M > 4.2\times$ for a pitch size of 15 µm and $\Delta x = 3.6$ µm), but this is wrong. According to Shannon's sampling theorem, at least two samples are necessary per spatial wavelength in order to have at least one pixel at the maximum and one at the minimum of the contrast, see Fig. 3.10a. Thus, for a pitch size of 15 µm and $\Delta x = 3.6$ µm, the lens must have a magnification of at least $M = 8.4\times$ for reaching the diffraction-limited spatial resolution. An even higher magnification factor may still improve the visual image quality, but for lock-in thermography, it also degrades the signal-to-noise ratio, which reduces with $1/M^2$ [101].

It is common in light microscopy to use high-NA objectives only for high magnification factors m, where this NA is necessary for obtaining the desired diffraction-limited spatial resolution. For low magnification factors, objectives of low NA are generally used. This has the advantage of a larger depth of field for low m, moreover low-NA objectives are cheaper than high NA ones, and the image brightness (which is proportional to the square of NA$/m$) may become independent on the magnification factor m. However, for thermal imaging of plane samples, this philosophy is clearly wrong. Here one is always interested in creating images with maximum possible brightness, and the depth of the field is not so important. For objectives, as well as for IR cameras, often instead of the NA the so-called f-number called $f/\#$ is given, which is the ratio of the distance to the diameter of the entrance pupil of the camera. This number governs the amount of light which can be fed through the objective to a camera. Values between $f/2 = 0.5$ and $f/1.5 = 0.666$ are typical for IR cameras. Ideally, the objective and the camera should have the same f-number. If the objective has a smaller f-number than the camera, the camera entrance angle is not fully exploited. Then, the thermal radiation that is not coming through the objective may enter the detector, which leads to an increased noise level. For a microscope objective having a magnification factor of m and a numerical aperture NA, the f-number is approximatively $f/\# = \frac{2}{m}$NA. Since the NA of an objective can hardly be larger than 0.7, for a magnification factor of $m > 2$, the lens anyway has a smaller f-number than the camera, hence it cannot fully exploit the sensitivity potential of the camera. Therefore, for any microscope objective with a magnification factor down to $m = 1$, the objective of a thermal imager should show an NA as large as possible for obtaining an f-number and thus a thermal sensitivity as good as possible. This means that, for magnification factors larger than 2, the diameter of the entrance lens of a microscope objective should at best have a diameter double of its working distance for obtaining NA $= 0.7$! If the magnification factor is small against 1 (conventional demagnifying objective), the f-number of the objective can and should always be chosen to match that of the camera.

One could ask now, why the refractive index n of the medium surrounding the sample stands in the denominator of (3.1). The reason is that the wavelength in a medium is proportional to $1/n$. Hence, immersing the object in a medium with high n is equivalent to imaging it in air with a lower wavelength. This is the reason why special immersion objectives, where the sample is embedded e.g. in an immersion oil having $n = 1.5$, are leading to a considerably improved spatial resolution in light microscopy. In principle, the same could be done for thermal microscopy. Unfortunately, water and also immersion oil is transparent neither in the mid nor in the long IR range. However, for samples with a plane surface (as ICs usually are) so-called solid immersion lenses (SIL) can be applied [103]. These are truncated bowls made from a transparent high-refractive index material, which are directly placed on top of a flat surface containing the structure to be imaged (see Fig. 3.11). Since only the innermost part of the truncated bottom face is optically used, the originally hemispherical SILs are often cone-shaped towards the bottom. This allows e.g. to place the SIL closer to bond wires. In the infrared region, silicon ($n = 3.5$) is an especially appropriate material for SILs, but also GaAs ($n = 3.4$) is often used. Gemanium ($n = 4$) would be even better, but since it absorbs radiation with a wavelength below 1.6 µm it can be used only for thermal imaging and not for near-IR investigations. If the gap between the sample surface and the plane bottom face of the SIL is negligibly small, the surface can be assumed to be "immersed" in the material of the lens. The SIL works as a magnifying glass for the following optical imaging system, which explains the gain in spatial resolution. Depending on the thickness of the lens, there are two basic types of SILs, namely "hemispherical" or "centric" SILs and "aplanatic" or "super"-SILs (a and b in Fig. 3.11). The

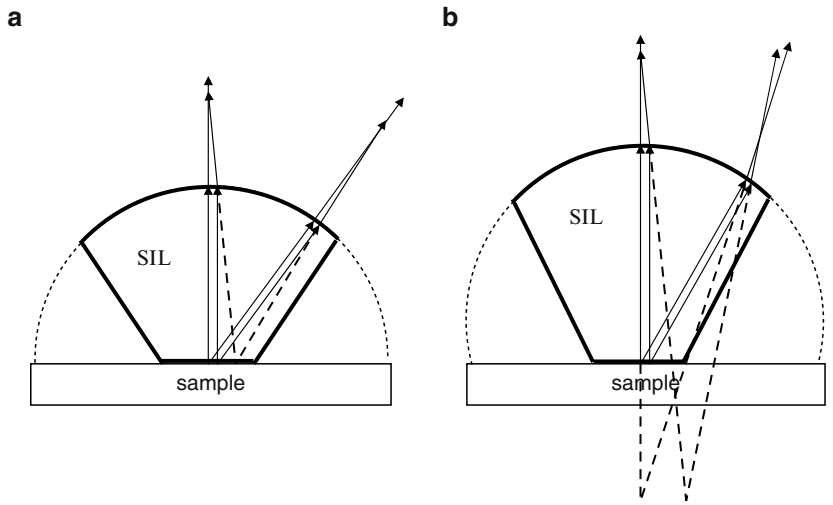

Fig. 3.11 (**a**) Hemispherical SIL and (**b**) "Super"-SIL with path of rays of a central point source (left) and an off-center one (right). Dotted lines: original bowl-shape before cone-grinding. Dashed lines: virtual path of rays (not to scale)

thickness d of the hemispherical SIL equals the radius R of the lens, whereas the optimum thickness d of the Super-SIL is [104]:

$$d = R\left(1 + \frac{1}{n}\right) \tag{3.2}$$

At this thickness the optical aberrations of a SIL are minimum, which is the basic advantage of the Super-SIL. However, there are more differences between both SIL types. As the path of rays in Fig. 3.11 shows, for a hemispherical SIL the virtual image is at the same depth as the object, whereas for the super-SIL it is lying considerably deeper. Also the magnification factors differ. For the hemispherical SIL, it is equal to the value of the refraction index n of the SIL material, but for the super-SIL it is about n^2. Nevertheless, in both cases the spatial resolution is limited by (3.1), whereby the angle of the light-emission within the SIL material is essential. For a hemispherical SIL the light emission angle within the SIL is the same as outside, but the super-SIL reduces it by a factor of $1/n$. So the following optics for a hemispherical SIL should work with a high NA, whereas that for a super-SIL is allowed to have an NA reduced by $1/n$. Of course, a SIL can also be used with a height smaller than its radius. In this case, its magnification factor and thereby its potential to improve the spatial resolution is smaller than n, and the virtual image is lying within the SIL-material.

Both super-SILs and hemispherical SILs may be integrated into a special SIL-objective, or they can be used as an add-on to a conventional microscope objective [105]. In this case, a special challenge is the positioning of the SIL in the middle of the image field. If an SIL is not cone-shaped towards the bottom as in Fig. 3.11, it can be slid into the desired position by using a mechanical aperture on top, which is connected to a micromanipulator [106]. As an alternative, Fig. 3.12 shows an SIL positioning facility, which can be used also for cone-shaped SILs and is available as an add-on to the 5× microscope objective of Thermosensorik (Erlangen) [19]. By using this facility, the user may first localize a hot spot without SIL and then, if the spot is in the middle of the image field, lower the SIL for a detailed inspection and remove it afterwards on demand. Since this is a hemispherical SIL, the focus position is at the same depth for working with and without SIL, and the high NA of the microscope objective is exploited. Meanwhile also other SIL positioning facilities are offered both by Thermosensorik [19] and Hamamatsu [20]. In Sect. 6.1 some results of the application of this SIL in IC failure analysis are presented.

An SIL can also be used for backside inspection by looking through the silicon bulk material of an IC. As Fig. 3.13 shows, there are different possibilities for doing that. In the simplest case (a) the backside is thinned down (for reducing the effect of free carrier absorption at high-doping levels of the bulk), carefully optically polished, and the SIL is placed on top of this backside. Since the remaining silicon substrate is also optically active, the desired thickness d of the silicon SIL has to be reduced for this application by the thickness of the bulk. This geometry has been called “Numerical Aperture Increasing Lens” (NAIL) [104]. This variant has the advantage that the SIL can be shifted to any position. However, the problem is to

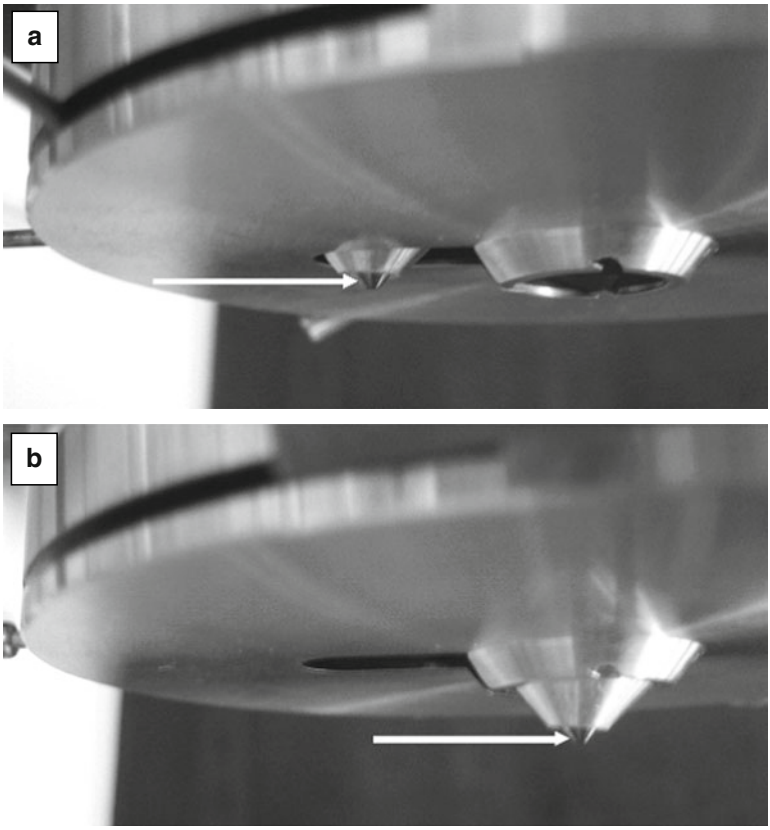

Fig. 3.12 (**a**) SIL positioning facility with SIL (see arrow) retracted and (**b**) in working position

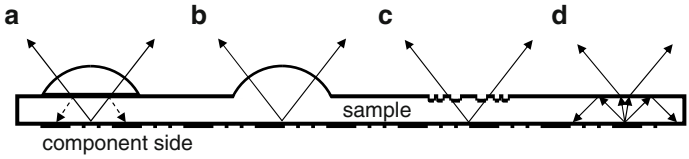

Fig. 3.13 SIL backside inspection: (**a**) NAIL, (**b**) FOSSIL, (**c**) diffractive SIL, (**d**) no SIL

flatten and polish the surface so accurately that the slit between surface and SIL is really negligible. If this slit is wider than a small fraction of the wavelength, total reflection prevents imaging with a high NA (see dashed arrows in a). Filling the slit with an immersion oil helps a little, but does not solve the problem completely since the refractive index of any immersion oil (typ. 1.5) is much lower than that of silicon ($n = 3.5$). This problem is avoided by machining the lens directly into the backside of the silicon wafer (b), as it was proposed by Koyama et al. [107]. The authors named this type of SIL "FOSSIL" for "FOrming Substrate into Solid

Immersion Lens". The basic limitation of this approach is that the position of a fault has already roughly be known by other investigations. Moreover, due to the finite thickness of the original substrate, the SIL can have only a certain maximum size, which limits the area that can be investigated. If the substrate is so highly doped that free carrier absorption becomes dominant, this approach is also not feasible. A similar SIL has been etched into the backside of a device by Scholz et al. by local Focused Ion Beam (FIB) etching with subsequent gas-assisted cleaning of the surface [108]. Since this technique does not allow the removal of large quantities of material, here a relatively shallow lens having a magnification factor of only 1.8 was produced. Another approach, which is also practical only for sufficiently transparent substrate and if the position of the fault is roughly known, is to machine a diffractive (zone) lens into the surface of the backside (c), as proposed by Zachariasse and Goossens [109]. By using local FIB etching and subsequent plasma etching, they produced a series of concentric ring-shaped grooves into the surface, which acts as a SIL. Though the light efficiency of this diffractive SIL was only about 15–20%, the gain in spatial resolution was impressive. Since the geometry of the diffractive structure depends on the imaging wavelength, and avoiding light losses is much more important for thermal imaging than for laser analysis, it still has to be proven whether this approach is feasible for thermal imaging also.

Even for backside inspection through a plane surface (Fig. 3.13d) the interesting region of an IC is immersed in silicon material, where the wavelength of light is considerably smaller than in air. Therefore one could argue that even in this case the spatial resolution could be improved compared to front side investigation. Unfortunately, this is not the case. As Fig. 3.13d shows, due to the high refractive index of the bulk, only light from a narrow cone within the material may exit the surface, whereas light emitted at a larger angle is totally reflected back. This completely compensates the effect of a smaller wavelength in the bulk material. In fact, regarding the law of refraction, in this case $\mathrm{NA} = n \times \sin(\theta)$ is the same inside and outside of the bulk material. Therefore backside inspection without an immersion lens (d) does not lead to any improvement of the spatial resolution. The use of solid immersion lenses (SILs), however, allows a decisive improvement of the spatial resolution by a factor of 3.5 (for a silicon SIL) for thermal imaging. Only this improvement allows to obtain a meaningful lock-in thermography results for failure analysis of modern integrated circuits.

3.5 Realization of CDI/ILM Systems

3.5.1 Absorption Mode

The first carrier density image published [12] was taken with an IR-camera without using the lock-in principle. Since this technique is not used anymore, we will here first discuss the setup published later including the lock-in technique [13] in some more detail.

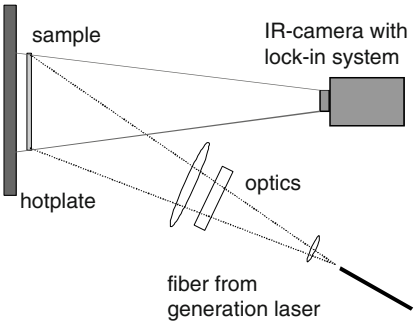

Fig. 3.14 Experimental setup for CDI/ILM measurements in absorption mode

This setup consists of a source emitting infrared radiation (hotplate), the sample under investigation exposed to this IR-radiation and an IR-camera (thermocamera) that measures the amount of IR-radiation transmitted through the sample (see Fig. 3.14). Additionally, a short-wave IR irradiation source is needed to generate excess free carriers, see Sect. 3.3. For a lock-in procedure a light source was needed that can easily be chopped with frequencies around 1–40 Hz and at the same time has a rise/fall time-constant below 0.5 ms. In the first version published, a fiber-coupled semiconductor laser with an optical output power of above 10 W was used to ensure an injection level in a $100 \times 100\,\mathrm{mm}^2$ sample that is about equivalent to the one obtained by full solar illumination (often called "1 sun" illumination). Present setups use lasers with a minimum optical output power of 2×30 up to 2×100 W and are able to homogeneously illuminate areas up to $21 \times 21\,\mathrm{cm}^2$. The illumination has to be as homogenous as possible. A semiconductor laser combined with optics that homogenize the irradiation to 5–10% non-uniformity and with a measurement of the generation distribution and a respective correction (see below) is appropriate. In newer systems, a non-uniformity of a few percent over large areas can be realized without rendering corrections. In the first setup, the homogenization was done in a similar way as in a solar simulator, present setups use commercially available homogenizers supplied e.g. by the company Limo [110]. The wavelength of the laser was chosen to be 917 nm (penetration depth $\alpha^{-1} = 40\,\mu\mathrm{m}$) to assure that only a negligible fraction of the light is transmitted to the rear surface of a typical wafer (thickness around 200 μm). A more efficient generation is obtained e.g. with a 940 nm diode laser, the penetration depth of 55 μm is still appropriate. Note that this illumination system for wafers (without the hotplate) is the same that can also be used for illuminated lock-in thermography (ILIT) on solar cells, see Fig. 3.6 in Sect. 3.3. Hence, by using such an illumination system, both ILIT on solar cells and CDI/ILM on wafers can be performed by one and the same system.

As the IR-source for the absorption mode a hotplate was used, that was homogenized by a thick copper plate on top coated with a black finish that has an IR-emissivity of about 0.96. The radiation intensity can thus be easily varied by adjusting the temperature of the hotplate. The camera detecting the IR-transmission

through the sample was in the first setup a mid-wave IR-camera based on a cadmium-mercury-telluride (CMT) focal plane array of 288×384 pixels. The noise equivalent temperature (NETD) was about 20 mK and frame rates of about 150 Hz were reached under typical measurement conditions. The camera was integrated in a Thermosensorik TDL 384 system (see Sect. 3.2), which connects the camera to a PC and allows the parallel application of two correlation functions to the data collected by the camera. The system also provides a square pulsed trigger signal with a fixed phase relative to the correlation functions, which can be used to trigger the light source. More recent realizations use e.g. a CEDIP Silver camera with 400 Hz frame rate [24].

In common to all setups is that, as for lock-in thermography, the correlation functions are chosen to be $K^{0^\circ} = 2\sin(\omega t)$ for the 0° Image and $K^{-90^\circ} = -2\cos(\omega t)$ for the −90° Image (see Sect. 2.2). This allows for the separation of the non-thermal (CDI/ILM) and the thermal signal. The non-thermal signal, which is proportional to the density of excess free carriers $\Delta n(t)$, has a response-time to the excitation $G(t)$, which is of the order of the carrier lifetime, thus about 1–1000 µs. So the non-thermal signal is fast compared to the lock-in cycle duration which is typically of the order of 25–1000 ms and the time interval between two pictures taken by the camera (typically about 6 ms for a frame rate of 166 Hz). Thus it can usually be assumed that the excess carrier density $\Delta n(t)$ is in-phase with the modulated excitation $G(t)$. Hence, this type of measurement is performed under quasi-steady-state conditions. If a thermocamera that takes images in a time distance in the order of microseconds would be available, then a small phase shift between the excitation $G(t)$ and the electric signal $\Delta n(t)$ could be observed, which could be used to obtain time-dependent free carrier information. A frame rate of the camera of about 10^5–10^6 Hz, that corresponds to this requirement, is at the moment far away from any technical possibilities. So at present, the non-thermal signal $\Delta n(t)$ and thus also the IR absorption of free carriers is generally taken to be exactly in-phase with the excitation $G(t)$ and to completely contribute to the 0°-image only. An approach, which nevertheless uses the build-up time of the carrier density in a square wave-shaped generation sequence will be discussed in Sect. 3.5.3.

The thermal signal, on the other hand, is 90° out-of-phase with its excitation, because the energy flow into the sample $P(t)$, which is in-phase with the generation $G(t)$, is essentially proportional to $\frac{\partial T}{\partial t}$ (with $T(t)$ the sample temperature), resulting in $T(t)$ being delayed by 90° compared to $P(t)$ for a periodic signal (see discussion of a spatially extended homogeneous heat source in Sect. 4.4). Thus the thermal signal of a homogeneously heated sample contributes to the −90° image and does not contribute to the 0° image.

Thus, using two correlation functions which produce a 0° and a −90° image allows separating the thermal and non-thermal (CDI/ILM) signal. In contrary to the thermal imaging, for CDI/ILM the 0°-image is exclusively used for calculating $\Delta n(x, y)$.

3.5.2 Emission Mode

An initial realisation of the emission mode was reported using a black background which was homogeneously cooled by Peltier elements [55] using the setup depicted in Fig. 3.14 with temperature of hotplate lower than wafer temperature.

To ensure that emission of the free carriers was dominating for the chosen background temperature of 1 °C, the power of the emitted radiation of the background at 1 °C was estimated and found to be only 36% of the emission of a background at room temperature and only 13% of the emission of the background used for the absorption CDI/ILM, which was usually at around 60°C. By this means infrared transmission through the sample is suppressed to a low level to prevent a superposition of the absorption signal and the signal coming from the emission of excess carriers. With this setup the transition between dominating absorption and dominating emission as theoretically calculated in Fig. 2.15 was quantitatively confirmed. A measured dependence of the camera signal on the temperature of the background T_b with the temperature of the wafer T_w kept constant was reported in [55] for a surface-passivated silicon wafer with a carrier lifetime of approximately 50 µs and is given in Fig. 3.15a.The fit was calculated from (2.23) with T_w (and thus the emission term) kept constant. The theoretical curve is confirmed by the measurement except for minor deviations attributed to condensation and ice on the sample. The result for the variation of the wafer temperature T_w and T_b kept constant also follows the emission part of (2.24) (Fig. 3.15b), with minor deviations for the range with small temperature differences.

A different approach to realise the emission mode was suggested in [57], with a respective setup presented in [56]. In this setup the wafer is placed on a metal surface having a high reflectivity and thus a low emissivity in the IR-range detected by the camera (see Sect. 2.1), e.g. a gold-plated mirror. This setup has distinct advantages compared to the low temperature background plate. By heating the mirror chuck, the wafer may be heated and at the same time a low IR emission from the background is maintained. In addition, the emission of the free carriers themselves is intensified by the back-reflection of the emitted radiation by the mirror surface. A scheme of a respective setup is given in Fig. 3.16 [56]. Here the focal plane array infrared camera used had a maximum sensitivity at 8.3 µm (long-wave), a frame rate of 38.9 Hz and an array size of 640 × 486 pixels. Excess carriers were generated by an array of 700 light-emitting diodes (LEDs) emitting at 880 nm and providing an excitation level equivalent to 1 sun. In [56] also a detailed treatment to quantify the sensitivity of the measurement with the setup in Fig. 3.16 by defining a noise equivalent lifetime (NEL) may be found.

3.5.3 Lifetime Calibration

To calculate lifetimes from the data obtained in a steady-state measurement, it is necessary to convert the camera signal that comes in "*digits*" or in units of

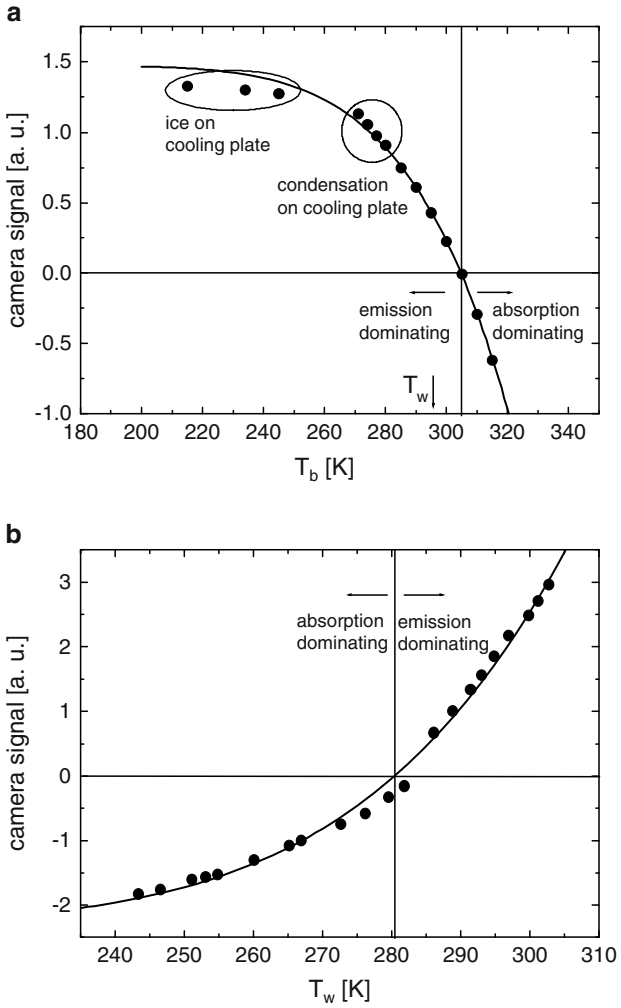

Fig. 3.15 Experimental confirmation of the transition between emission and absorption mode for (**a**) variation of the background temperature T_b with the temperature of the wafer T_w constant and (**b**) variation of T_w and T_b constant. Calculated lines are according to (2.23) and (2.24)

millikelvin to excess carrier densities Δn. These are then transformed to excess carrier lifetimes using (2.20) and the local generation density G determined experimentally (if non-uniformity is pronounced) for the respective setup. For this lock-in technique, a differential calibration transforming Δ *digits* to Δn is sufficient. The general approach to do this was developed by Bail et al. [12]. The practical details given in the following are for the setup shown in Fig. 3.14 and taken from [53].

The basic calibration idea is to use a set of FZ-wafers which have different doping levels but are otherwise identical between each other and also identical to the

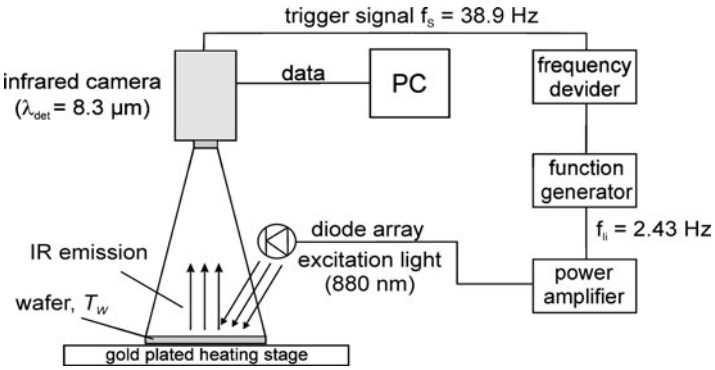

Fig. 3.16 Setup to obtain a lifetime image in emission mode using a gold-plated heating stage [56]

wafer to be measured. This regards not only the wafer thickness but also the state of roughness of the surface. Note that this roughness, by determining the degree of light scattering, also determines the average length of the light paths in the wafers. These wafers are successively put between the camera and the hot plate for measuring their transmissivity in steady-state mode. The differences observed are then due to the differences in free-carrier absorption of the samples. The obtained data can be fitted linearly, since the changes in transmissivity due to free-carrier absorption are small. An example of a plot of the transmissivity in camera digits over wafer doping density for an absorption-CDI setup is given in Fig. 3.17. Here the calibration results in a slope of the linear fit of $m = -(3.82 \pm 0.16)10^{-13}$ digits cm^2 for the camera module used. This slope can then be used to transform the camera signal Δ *digits* into excess free carrier concentrations by the relation:

$$\Delta n(x, y) = \frac{\Delta\, digits(x, y)}{m\sigma W}\zeta. \tag{3.3}$$

Here W is the wafer thickness and σ is a correction factor taking account of the fact that in the calibration procedure p-type wafers were used and thus only the IR absorption of holes has been measured, but that in a real measurement due to electron hole pair generation the free carrier absorption of holes and electrons has to be taken into account (see (2.20)).

The free carrier absorption in silicon was experimentally found to be [46]:

$$\begin{aligned} \alpha_{\mathrm{n}} &\approx 1 \times 10^{-18}\lambda^2 n, \\ \alpha_{\mathrm{p}} &\approx 2.7 \times 10^{-18}\lambda^2 p. \end{aligned} \tag{3.4}$$

Here $\alpha_{\mathrm{n,p}}$ is the absorption coefficient for electron/hole free carrier absorption, respectively, λ the wavelength and n/p the free electron/hole density. Thus σ is given by $\sigma = \frac{2.7+1}{2.7} = 1.37$. ζ is another correction factor taking into account the difference between the "real" camera contrast between illuminated and

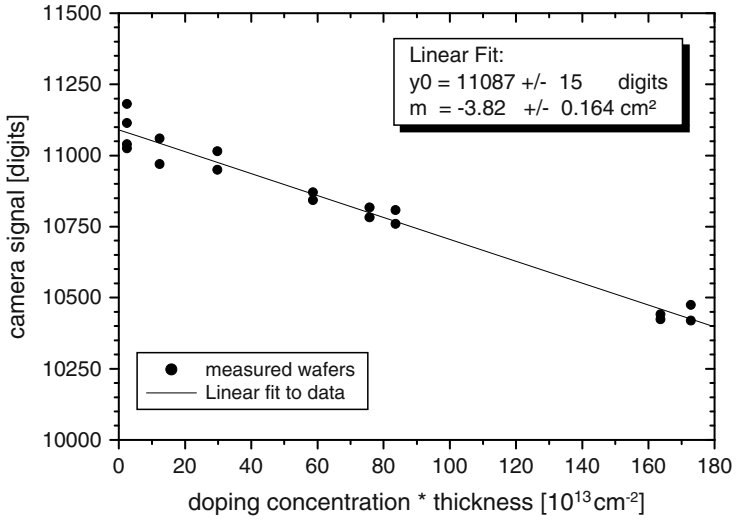

Fig. 3.17 Calibration of the camera signal for excess carrier densities Δn via a set of differently doped mono-crystalline wafers

unilluminated state and the signal given by the lock-in correlation. In the case of a correlation function of $K^{0^\circ} = 2\sin(\omega t)$ it results in $\zeta = \pi/2$. In (3.4) it is assumed that sensitivity differences between the camera pixels are already corrected, e.g. by a 2-point correction procedure.

Actual diode laser irradiation systems reach already uniformed irradiation with deviations of a few percent only, which may then be included in the measurement uncertainty. If the inhomogeneity of the irradiation is significant compared to the desired measurement accuracy, the local excess carrier lifetime calculated from the measured $\Delta n(x, y)$ images from (2.19) written for each pixel $p(x, y)$ has to be corrected in addition accounting for the variable $G(x, y)$. The semiconductor lasers used for irradiation are in general very stable sources. Thus it is possible to map the generation irradiation $G(x, y)$ once during the setup phase of an individual system and use it for subsequent measurements.

A calibration with a set of planar wafers results in absolute carrier lifetimes for measurements on a planar (untextured) wafer. With the same calibration, measurements on textured wafers lead to unrealistically high lifetimes and a blurred appearance of the image. This may be interpreted as follows: for a planar wafer, the radiation emitted by an excess carrier can leave the silicon only within in a small cone of about 17° width. Due to the high refractive index ($n_{\mathrm{Si}} = 3.4$ for $\lambda = 4\,\mu\mathrm{m}$), radiation emitted under higher angles is internally reflected and not detected by the camera. A rough surface allows a larger part of the total radiation emitted by free carriers to exit the silicon toward the camera aperture. For a certain carrier density, a higher signal results as compared to the calibration situation, which mimics a higher carrier lifetime. In addition, at a specific position, radiation not only from this wafer

segment but also from neighbouring parts of the wafer may be detected, which leads to blurring.

A solution for the spurious lifetime increase would be the calibration with a set of wafers with the same type of surface roughness as the one of the sample under test, which is tedious to do and sometimes not possible. Another solution was proposed in [111]. A local emissivity correction is deduced from the slope of the increase with temperature of the emitted photon density compared to blackbody radiation. For the emissivity correction, only the topography images at room temperature and at the elevated measurement temperature are needed.

As a second correction step, in [111] a deconvolution is suggested, in order to convert the blurred measured lifetime distribution to the actual distribution. In [111], a suitable point-spread function and a Fourier transformation with a Wiener filter were used. The procedure was found to be fairly insensitive to the exact shape of the point-spread function. The shape given in [111] was based on an experimentally determined distribution.

With both steps, emissivity correction and deconvolution, the carrier lifetime image obtained from a textured wafer was demonstrated in [111] to closely resemble the one obtained from a neighbouring wafer (within a multicrystalline block) prepared with planar surfaces. An extensive treatment of deconvolution techniques with emphasis on thermal images is given in Sect. 4.5.2.

Although the time resolution of thermal cameras is at present not sufficiently high for directly measuring the time-dependence of free carrier generation, the lag in build-up and decay of the carrier density compared to the rise and fall of a fast-switching generation source can be used for a direct dynamic determination of the carrier lifetime. This allows a lifetime calibration of CDI/ILM images independent of signal intensity, i.e. especially of optical sample properties ("dynamic ILM" [40]). The method to retrieve this information from a sample subject to a square-shaped generation G is sketched in Fig. 3.18. Here images with a short integration time are taken, which allow to compare the local carrier concentration during the build-up (first image) with the steady "on"-state (second image). The third and the fourth image are used for background correction within a lock-in procedure. To achieve a sufficient difference between the first two images, which directly relates to the accuracy in determining the carrier lifetime, a sufficiently short integration time t_{int} has to be chosen. The sequence plotted in Fig. 3.18 is used for an implementation of a lock-in procedure. For details, how the carrier lifetime is deduced, we refer to [40]. Using the 4-point correlation (see Sect. 2.2) a relation of the phase Φ (see (2.8)) with the carrier lifetime is deduced [40]:

$$\Phi = \arctan\left\{\frac{t_{\mathrm{int}} - 2\tau_{\mathrm{eff}}\left[\exp\left(-\frac{T}{4\tau_{\mathrm{eff}}}\right) - \exp\left(-\frac{T+4t_{\mathrm{int}}}{4\tau_{\mathrm{eff}}}\right)\right]}{t_{\mathrm{int}} - 2\tau_{\mathrm{eff}}\left[1 - \exp\left(-\frac{t_{\mathrm{int}}}{\tau_{\mathrm{eff}}}\right)\right]}\right\}. \tag{3.5}$$

For a reasonable integration time $t_{\mathrm{int}} = 300\ \mu\mathrm{s}$, an approximately linear relation of phase Φ and lifetime τ_{eff} is found for carrier lifetimes below about 200 µs. With a lock-in frequency of 40 Hz (period length $T = 25\,\mathrm{ms}$) dynamic ILM images on

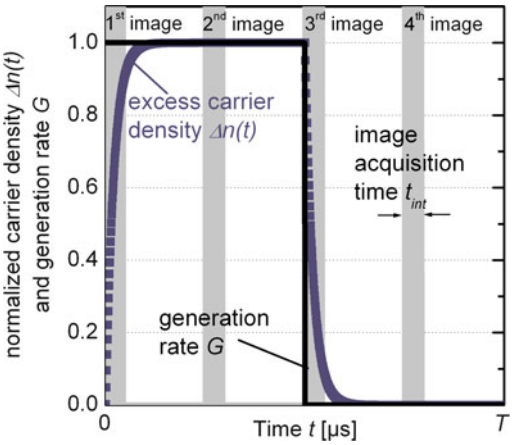

Fig. 3.18 Timing sequence used in dynamic ILM (courtesy of K. Ramspeck, ISFH Hameln)

surface-passivated multicrystalline wafers could be obtained within 1 s, with absolute values agreeing well with microwave detected photoconductance decay maps. The image obtained from the method presented in [40] was found to be hampered by blurring. In a successive publication [112], the higher sensitivity to blurring effects was attributed to the stronger impact of laterally guided radiation on the dynamic evaluation as compared to standard CDI/ILM. The main application of this technique is seen in an independent scaling procedure for conventionally measured CDI/ILM images, which show a better spatial resolution. The approach to use combined dynamic and steady-state images was exploited further in [112]. Phase effects due to the heat signal induced by the optical excitation have to be corrected. Otherwise they may lead to high errors especially for lifetimes approaching the detection limit of the technique (about 10 µs stated in [112]). If the areas of highest lifetimes (50 µs in the example) of a heat-signal-corrected dynamic ILM measurement are used to calibrate a steady-state CDI/ILM image, excellent agreement with a (area averaged) QSSPC measurement was demonstrated. Note that this approach intentionally exploits the irregularity of the phase measurement for 4-point correlation and square-shaped signal, which was mentioned already for Fig. 2.9 in Sect. 2.5.